In-beam spectroscopy of ^{72}Ge

Katharine Rose Henninger

Thesis presented in fulfilment of the requirements
for the degree of Masters of Science at Rhodes University

Supervisor: Dr D. G. Roux
Department of Physics
Rhodes University

August 2011

Declaration

I, the undersigned, hereby declare that the work contained in this thesis is my own original work and that I have not previously, in its entirety or in part, submitted it at any university for a degree.

Signature:..

Date:...

Abstract

The high-spin states of the nucleus ^{72}Ge were populated via the ^{70}Zn(α,2n)^{72}Ge fusion-evaporation reaction at a beam-energy of 30 MeV. The γ-decays were observed with the AFRODITE spectrometer array at iThemba LABS (Faure, South Africa). Twenty-seven new transitions, 18 new levels and 2 new bands were added to the ^{72}Ge level scheme, and several corrections were made to the previously-known level scheme. Transitions were characterised using Directional Correlation from Oriented states (DCO) and polarisation measurements, and spin-parity assignments were made for 7 new levels. Spin and parity were also reassigned to a previously-known structure. One of the new bands was identified as part of an octupole-vibrational band. No tetrahedral states were observed in the scheme despite N=40 and Z=32 having been identified as tetrahedral magic numbers. The meaning of the new 14^+ yrast level for the underlying structure of the ground state band is discussed.

Acknowledgements

There are so many people to whom I owe a debt of thanks that I feel this work should be much larger in scope to do their contributions justice!

Firstly, to the late Prof. Paul Nathanson, without whom I would not be doing Physics at all: Thank you for believing in me, giving me confidence, and for being my example of a physicist. Thanks for keeping me in Physics also go to Prof. Steven Karataglidis: Thank you for hours of Maths tuition and for much support and encouragement.

A huge debt of gratitude goes to my supervisor, Dr David Roux. I value your patience, guidance and expertise as much as your support and sense of humour. Thank you for so much.

Thanks to Dr Rob Bark for widening my horizons and for patient assitance even with daft questions! Thanks also to Dr Elena Georguieva-Lawrie for important tuition, and to Sean Murray for invaluable technological help. Thank you to Prof. Pat Terry, for believing in me, and to all who taught me Physics at Rhodes: especially Dr Ray Haggard, for kindness and valuable lessons, and Dr Jennifer Williams, for sharing her insights.

To my mother, who opened my mind and taught me how to think: I would not see things as I do without your having been my first teacher. I cannot thank you enough for your support, love and guidance throughout this work, and before.
To Helen: my example and source of strength, my guiding light and my friend. Nothing would have got done, or been worth doing, without you.
To my father: thank you for support and tolerance, and for your guidance in the thesis-writing jungle.
To my grandmother: thank you for teaching me about spectra, for sharing your experiences, and for being my example of a female scientist.

Thank you to all, (those mentioned and those not), who have supported me, taught me and encouraged me during this work: neither it nor I would be much without you.

The financial support of the NRF and NITheP is gratefully acknowledged.

Contents

List of Tables

List of Figures

1 Introduction

The shape of nuclei, and how this is related to proton and neutron number, is an important key to the nature of the internucleon interaction, as the states which nucleons can occupy when in the presence of other nucleons is what ultimately determines the nuclear shape. As such, nuclear deformation is an important field of study in both experiment and theory.

While nuclei can in essence assume all manner of spheroidal shapes, most nuclear models are truncated at quadrupole ($\lambda = 2$) deformation, there being very few cases in which deformation beyond $\lambda = 2$ is encountered. Recently, however, research in collective behaviour has been directed towards modelling octupole- and higher collectivity; mainly because neutron-rich nuclei are likely to show such "exotic" deformation [1]. One of these new models predicts the existence of static tetrahedral deformation at certain "tetrahedral magic numbers" of protons and neutrons [2]. According to these predictions, ^{72}Ge should display tetrahedral excited states, since it possesses tetrahedral magic numbers of both protons and neutrons [2].

The nucleus ^{72}Ge is a particularly interesting one, as many unusual phenomena have been postulated at the proton- and neutron-numbers $N = 40$, $Z = 32$, especially when the systematics for the $Z = 32$ nuclei are considered. Experimental phenomena observed here are variously attributed to change of ground state deformation, static octupole collectivity, coexistence of a highly-deformed shape, and a particularly strong p-n interaction [3-8]. There is added interest brought about by the postulated shell closure for $N = 40$.

As yet, neither the predictions of static octupole deformation associated with the 3_1^- level [4] nor possible shape coexistence [5] nor the proposed shape underlying the ground state band have been experimentally tested. Given the current interest in octupole- and higher deformation, verification of possible static octupole deformation modes in ^{72}Ge [4,9] would be of interest to the field.

The aim of this project is to extend the level scheme of ^{72}Ge using gamma-gamma ($\gamma-\gamma$) coincidence data, with the aim of verifying some of the predictions made for this nucleus. Observation of "tetrahedral bands" (low-lying, negative-parity bands with no intra-band $E(2)$ transitions [1]) during this process would help to verify the tetrahedral model of [2]: thus, aiding the verification of this model is a secondary aim.

The current level scheme of ^{72}Ge [10,11] essentially comprises five major bands, all fairly well-understood in terms of the structures they represent. It is likely that the intra-band transitions of tetrahedral bands will be low-intensity, since tetrahedral states are likely to be poorly populated. Previous experiments [10,11] were not suitable for the detection of low-intensity transitions, making tetrahedral bands unlikely to surface in the previous level schemes and making it necessary to enlarge them using more extensive $\gamma-\gamma$ data for this prediction to be verified.

At the current time, much work has already been carried out with the aim of finding tetrahedral bands. *e.g.* the most recent extension of the level schemes of tetrahedral candidates ^{156}Gd and ^{160}Yb [12]. Investigations have, however, not yet found any concrete evidence of such bands: the low-lying negative-parity bands located in nuclei ^{156}Gd and ^{160}Yb, for example, proved to contain $E2$ transitions between higher-spin levels, and as such were interpreted as octupole vibrational bands.

As there is an enhanced probability of $E2$ transitions for ^{72}Ge brought about by high occupancy of the $g_{\frac{9}{2}}$ orbital [8], and the nucleus is, according to most accounts, only slightly deformed in the ground state [13], its behaviour is likely to be almost purely vibrational, or at best "intermediate between a vibrator and rotor" [14]. Thus, if there is octupole collectivity, it seems quite likely that it would take the form of octupole vibrational bands rather than permanent deformation, (despite predictions of static octupole deformation); a phenomenon also observed in other tetrahedral candidates [12].

As nuclear deformation is ultimately a result of the internucleon interactions and how they shape both the mean field and residual interactions, the ultimate goal of research into deformed nuclei should be to learn about the internucleon interaction and its various dependencies. Thus, a major priority of experimentation should be to interface with the theory describing the underlying nucleon distributions and interactions, to allow information to increase knowledge about these phenomena. This project hopes to at least in a small way to interface between experiment and theory, both by testing this new model, and, where possible, by interpreting the results using both macroscopic and microscopic approaches to look at the underlying causes for the overall behaviour.

2 Background

Nuclear deformation was first encountered in the 1930's via measurements of hyperfine structure phenomena in the optical spectra of (among other nuclei) ^{151,153}Eu [15]. To date, many models (both macro- and microscopic) have been devised to describe and analyse deformation. The list includes the Particle-Rotor model and the Vibrational model (collective models), while single-particle approaches include large-basis- and projected- Shell-Model calculations, the Nilsson Model and the Cranked Shell Model.

The Bohr model [16] was the first collective model to include deformation. It introduced the (now standard) idea of a deformed nucleus as a deformed core, coupled to any unpaired nucleons; the shape of the deformed core being expressed by the equation for the nuclear radius [16]:

$$R\left(\theta,\phi\right) = R_0\left[1+\alpha_{\lambda\mu}Y_{\lambda\mu}\left(\theta,\phi\right)\right]. \tag{1}$$

The equation expresses the nuclear radius R as a function of the polar and azimuthal angles θ and ϕ. The parameters $\alpha_{\lambda\mu}$ characterise the shape of a multipole, single-particle potential $U(\vec{r})$, in which the nucleons move [17].
It is the shape of this potential well that dictates the nuclear shape. Because of this, the symmetry of the potential well thus dictates the nuclear symmetry, so that altering it will change the symmetry of the nuclear shape [18]. Thus, in calculation, it is feasible to alter the symmetry of the potential well so that the nuclear shape resulting from it has other symmetries. In this manner, any models based on the above parameterisation may be extended to model deformed nuclei of almost any symmetry, depending on the terms included.

The recent work by Dudek *et al.* [1,2,19,20] follows this route of altering symmetry of the potential well. In this approach, a nuclear Hamiltonian is created by extending an existing Hamiltonian to alter its symmetry group to that of an octupole-deformed object (see [2]). This concept applies equally well to macroscopic or microscopic Hamiltonians: some papers [2,19] extend the Rotor Hamiltonian $H = \sum_{i=1}^{3} \frac{\hbar^2}{2\mathfrak{J}_i} I_i^2$ thus, and others [1] start from various microscopic Hamiltonians. The microscopic approach was used to find energy minima at different N and Z values, giving the "tetrahedral magic numbers" at which tetrahedral deformation is expected. These have as yet not been experimentally verified.

The tetrahedral model was originally postulated to explain the very low-lying "octupole vibrational bands", with apparently vanishingly-weak intra-band $E2$ transitions, observed in the early rare-earth nuclei [21]. Some of these assumed cases of tetrahedral deformation have been recently explored (notably ^{156}Gd and ^{160}Yb [12]). In these cases [12], there has been no evidence observed of the existence of tetrahedral shapes; but more evidence is still needed to conclusively confirm or refute the tetrahedral model.

Aside from being a tetrahedral candidate, the nucleus ^{72}Ge has generated much interest in general, due both to the postulated shape coexistence and the lowering of the 3^-_1 and first 0^+ levels at $N = 40$, $Z = 32$. The nucleus is doubly-even and medium mass, has a moderate ground state deformation ($\beta = 0.074$ [22], or $\beta = 0.242$ [23].[1] The ^{72}Ge ground state is described as "intermediate between a vibrator and rotor" in structure [14]. There have been many studies (both experimental and theoretical) of this nucleus, each using different approaches, but none have yet recorded a band with tetrahedral characteristics, and there exists to date no collated work which attempts an overview of this rich and interesting nuclear system. The studies done to date are tabulated below, with a summary of their results (Table 1).

---

[1] the larger value of $\beta = 0.242$ was determined via calculation [23] and is considered incorrect by [24].

Table 1: Studies of ^{72}Ge to date, listing most important findings.

Study	Findings	Reference
$\gamma-\gamma$ coincidence measurements from fusion-evaporation reaction	Level-scheme of ^{72}Ge; characterisation of 33 transitions.	[10]
$\gamma-\gamma$ coincidence measurements following β-decay of ^{73}Ga [14] and β-decay of ^{72}As [11]	Extension of ^{72}Ge level scheme; observation of 0^+_1 state.	[11,14]
^{74}Ge(p,t) reactions	DWBA analysis of several band-heads, prediction of energy of low-lying 0^+ excited state (690 keV).	[7]
Electron-scattering from ^{72}Ge	Prediction of energy of low-lying 0^+ state (690 keV), and of a possible deformed band built on it.	[5]
Coulomb excitation of ^{72}Ge	The transition between 0^+_1 and 2^+_1 failed to be observed. Discussion of octupole collectivity based on measurement of 3^+_1 energy.	[5]
Large-basis shell-model calculations	Calculation of $B(E2)$ values for $^{66-76}$Ge; noted enhanced $B(E2)$ values for ^{72}Ge. High $g_{\frac{9}{2}}$ occupancy used; gives good prediction of 2^+_1 and 3^-_1 energies. Large p-n interaction proposed.	[8]
Projected shell-model calculations (PSM)	Calculation of yrast level energies up to 10^+ [14]; calculations over-predict energies above 4^+.	[14]

Continued on Next Page...

Table 1 – Continued

Study	Findings	Reference
Projected shell-model calculations (PSM)	Prediction of possible static octupole deformation through calculating 3_1^- energies. Prediction of back-bending at 14^+ yrast level as an indication of prolate shape for the ground state band.	[3]
Interacting Boson Approximation (IBA) calculations	Investigation of possible static octupole deformation; finding that a configuration of 10 *s*-*d* bosons and 1 *f*-boson best describes experimental observations of 3_1^- level and $B(E3)$ values. A configuration of 10 *s*-*d* bosons and two fermions was found to better describe behaviour at higher angular momentum.	[4]

Figure 1: The previously-known ^{72}Ge level scheme [10]. Intensities (except for that of the 834 keV transition) are indicated by arrow-width, and were fitted using the data from our experiment. Note the low-lying 3_1^- level, and the structure built on it (band 6).

At the time this study was undertaken, two level schemes for ^{72}Ge had been produced: the original one [10] which is supplied, converted to standard format (Fig. 1); and the recent update of [14].

The studies all reveal, as mentioned, interesting changes occuring at $N = 40$, $Z = 32$ in the systematics for Ge isotopes; mainly lowering of the 3_1^- and first excited 0^+ states. Some (notably [4]) also suggest the opening of a shell-gap here, and note the possibility of a strong p-n interaction with this combination of N and Z as being responsible for the observed lowering in energy of the $g_{\frac{9}{2}}$ orbital [8].

3 Theory

3.1 Nuclear shape and collective behaviour

The shape of a nucleus is the cumulative result of the distributions of all the nucleons in the system [17]. These distributions depend on the nuclear potential V, which itself derives from the interaction of each nucleon with every other in the system, as in the Hamiltonian [17]:

$$H = T + V = \sum_{i,j=1}^{A} T_{ij} a_i^\dagger a_j + \frac{1}{4} \sum_{ijkl} V_{ijkl} a_i^\dagger a_j^\dagger a_l a_k, \tag{2}$$

where $a^\dagger$ and a are particle creation and annihilation operators, and the sums are over all possible (single-particle) states in the nucleus.

Nuclear shape follows naturally from this Hamiltonian (Eqn 2), as it dictates the overall wavefunction Ψ. Shape is thus dependent on the state of every nucleon present. The Hamiltonian also has an implicit dependence on N and Z, as these affect the number, and nature of, interactions each nucleon feels [25], and thereby affect the potential V. Thus, nuclear shape varies with N, Z and excitation.

As the behaviour of this many-body system is impossible to solve for exactly, the Hamiltonian is often made solvable by adopting a single-particle view: approximating the V each particle feels with a mean field U, in which each particle is considered to move independently of all the other particles. The difference between U and the "true" interaction (V) for any particle is then the residual interaction, $(V - U)$, which contains any interdependence of the nucleons' states unaccounted for by the approximate mean field potential U.

The appropriate U to use is a reflection of underlying interactions, as, due to its dependence on N, Z and excitation, one can consider that V (for each nucleon) will vary with these properties, making the appropriate U to approximate it also vary.

In order to make sense of experimental observations and use them to understand the underlying behaviour of the nucleons, predictions of energies for excited states are compared to measured excitation energies. The potential and configuration mixing used in the calculations affect how well the predicted energy-levels and measured excitation energies coincide. Good predictions thus indicate that the interaction and model-space used are a fair reflection of actual nucleon behaviour, and insight is gained. The only drawback to this approach is the necessary truncation of the model-space, which may limit the accuracy of the predicted energies for states more collective in nature.

It is known that the shell-model potential is a good approximation to V when N and Z are shell-model "magic numbers", and the nucleus is in its ground state. However, if N and Z deviate from the shell-model magic numbers, or the nucleus is produced in an excited state, V deviates from this "ideal" U, and becomes such that the associated overall nucleon distribution is anisotropic, giving rise to deformed nuclei. The effect of this change in V may be included in the single-particle shell-model to some extent by configuration mixing, or may be included implicitly by moving from a single-particle model to a collective one.

In addition to permanent deformation (for which the symmetry of the potential well U dictates the symmetry of the arising nuclear shape [17]), there may be periodic changes in the overall nucleon distribution. At a certain energy, the valence nucleons may oscillate between two possible distributions, due to configuration mixing, and when the correlations between these and other lower-energy orbitals are strong enough, the motion may be highly collective. Periodic changes in radial distribution are vibrations; in angular distribution, rotations. These motions are the outcome of the residual interaction $V - U$ and the resulting correlations [25]. Both motions will impart an additional angular momentum to the nucleus.

While these behaviours have their origin in microscopic phenomena, they are generally discussed in macroscopic terms. Generally, macroscopic models consider that the nucleus behaves as a macroscopic core, made up of pairs of nucleons, coupled to any odd nucleons. The understanding of nucleon behaviour gained in such an approach is somewhat more indirect than via a microscopic approach, but it yields much useful information, such as: An indication of the strength of the residual interaction; at what energies certain single-particle states become accessible; the nature of the correlations, and any sudden raising or lowering of the energies of states. How these are elucidated macroscopically is discussed briefly below.

It is obviously necessary to consider collective behaviour collectively; as an overall rotation or vibration. Macroscopic discussions of vibration or rotation may tell one about properties like the accessibility of various Nilsson states, the energies at which single particles move into new orbits, and configuration mixing with intruder orbitals. Vibration and rotation are discussed in later sections (Section 3.6 and 3.7).

Macroscopic descriptions of coupling between extra-core nucleons and the core also reflect long-range correlations. Either the core dictates the allowed distributions of the valence nucleons, but in all other respects rotates independently of them (deformation-aligned coupling (DAL)); or the rotation of the core and the unpaired particle(s) may be coupled (rotation-aligned coupling (RAL)) [31]. In DAL, interaction of the other valence nucleons with the odd nucleon re-shapes its orbit, so there must be strong long-range correlations which mix the valence orbitals. Thus, DAL is indicative of a more long-range interaction, such as could still be approximated by a mean field, since an appropriate mean field will account for these correlations. In RAL, the residual interaction links valence nucleons that lie adjacent to each other into more-or-less a pair, tracking the motion of each other. Thus, RAL is indicative of an interaction which may not be able to be averaged into the mean field, since it is specific to a few adjacent nucleons.

The accessibility and favourability of certain single-particle states is reflected by the alignments of the extra-core particles. The band-crossings with various quasi-particle bands indicate that, at the energy associated with the alignment, the states occupied in these bands become favourable and are mixed into the overall nuclear state by the potential V.

It must be remembered that, experimentally, the excited states of a nucleus are populated "in reverse": that is, the nucleus is created in its highest excitations via collision-and-fusion with an ion; and from there decays to its lowest-energy states. The nucleons thus initially experience a potential such as they would have at high excitation, and from there rearrange themselves as the potential allows, changing the potential and losing energy as they do so, until a state of minimum energy is reached. Only certain initial arrangements of nucleons are possible, and so, despite the number of possible collisions, only certain intrinsic arrangements are produced, which then decay to whatever minimum-energy state they are destined to reach by their initial, high-energy arrangement. These decay patterns from several highly-excited states to ground state are the bands recorded in the nuclear level scheme.

3.2 Fusion-Evaporation reactions

When a projectile and some target nucleus collide and fuse, the resulting system may either fission, or, if there are barriers to fission, evaporate excess nucleons and energy to form an excited nucleus that then decays to its ground state [26]. The latter scenario is a fusion-evaporation reaction. Fusion-evaporation reactions are the most appropriate for γ-ray spectroscopy, as the energy introduced to the system is low enough for γ-decay to be the main mode of de-excitation [27]. The following discussion of fusion-evaporation is mainly from [26] and [28].

Choice of reactants for a fusion-evaporation reaction generally depends on four things: the balance between fusion-evaporation and fission (determined roughly by considering the neutron-number of projectile and target nuclei); the probability of obtaining the desired product; the maximum amgular momentum of interest, and availability of beams, targets *etc.*[28].

The reaction cross-section $\sigma_{\beta\alpha}$ from the incident channel (here channel α) to the exit channel of interest (exit channel β) is given by [26]:

$$\sigma_{\beta\alpha} = \sigma_\alpha \frac{\Gamma_\beta}{\Gamma}, \tag{3}$$

where σ_α is the reaction cross-section for the entrance channel α, and $\frac{\Gamma_\beta}{\Gamma}$ is the decay probability for decaying through channel β. The size of the reaction cross-section will indicate the yield of some exit "product" from the initial reactants, allowing reactants to be chosen for maximum yield.

The transfer of energy to the system by a reaction depends on a number of factors, primarily energy and momentum of the projectile. The transfer of energy also affects which initial channels are populated, so projectile energy is chosen for maximum yield, usually via a Monte-Carlo-type simulation.

Immediately after the collision, the projectile-target system is simply a "composite system", consisting of excited protons and neutrons. This system will emit ("evaporate") excess neutrons and energy in the form of γ-rays called statistical γ-rays. A system is not truly a nucleus until it has stabilised to the point that its excess energy is taking the form of excited behaviour: rotations or vibrations, or single-particle excitations [29]: *i.e.* it corresponds to a nucleus in an excited state. At this point, the emission of γ-rays follows a definite cascade between nuclear excited states (see Fig. 2). The character of these "discrete" γ-rays is indicative of the nature of the states between which they occur, and they are recorded for construction of level schemes.

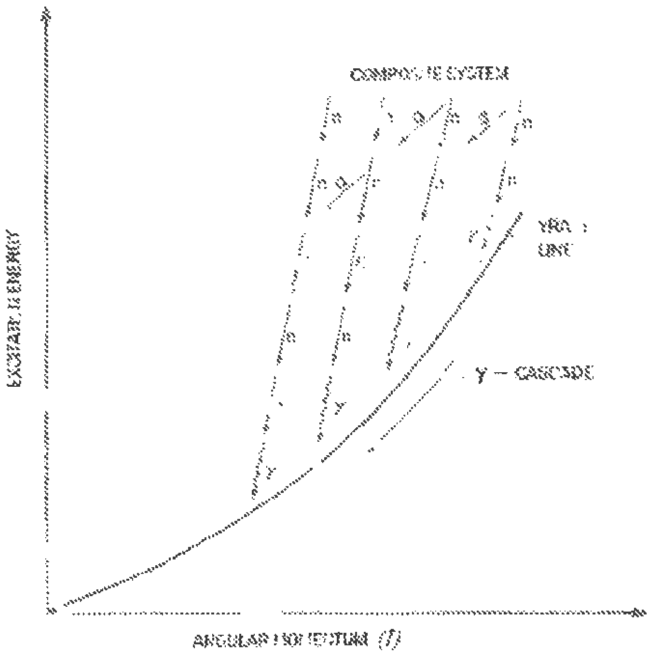

Figure 2: Schematic diagram of decay following a fusion-evaporation reaction, showing decays from systems of increasing angular momentum I. After the formation of the composite system, neutrons and statistical γ-rays are emitted before the nucleus becomes a system capable of emitting a discrete γ-cascade (diagram from [26]).

According to the N and Z of the nucleus created, different initial excited states will be possible. Each of these decay in a definite pathway (often a band of states) to the stable state most accessible from the initial state. The decay will usually proceed in such a way as to reach states of lowest energy for a given spin (an yrast level) before proceeding to the nuclear ground state. If the ground state is not accessible from the initial state, the nucleus will decay to some metastable state that is not the ground state: an isomeric state.

Initial states will be populated differently, as the angular momentum transferred in a collision depends on the perpendicular distance between the centre of force and the incident velocity vector: the "impact parameter", $\mathbf{b}$ (see Fig. 3). As $\mathbf{l} = \mathbf{b} \times \mathbf{p}$ ($\mathbf{p}$ is the linear momentum of the projectile), higher $\mathbf{l}$-values are transferred with greater $\mathbf{b}$. However, the arc-length of the sphere is greatest at the equator (where b is zero), and reaches a minimum for regions of greatest b. Thus, the probability of collisions with regions of large b is very small. High-I states are thus weakly populated and the intensity of transitions from them is low.

3.3 Modelling collective behaviour

Describing nuclear collective behaviour requires a two-pronged approach: a collective, large-scale overview of the situation, and a single-particle view in which the underlying framework and causes of those macroscopic characteristics are considered. Both collective (macroscopic) and single-particle (microscopic) models are used for deformed, rotating nuclei.

The macroscopic models include the residual interaction implicitly, while the microscopic models include an approximation to it explicitly, via whatever potential is used to approximate the interactions. Each model will interface

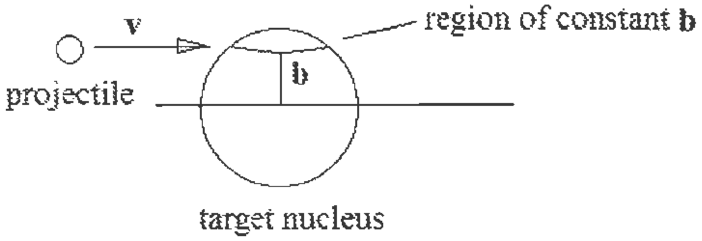

Figure 3: Illustration of impact parameter **b**. Note that **b** is zero for a collision at the equator, and reaches a maximum only for a collision with the end-points of the nucleus.

with different experimental observables [26], depending mainly on what they are used to predict, and what view of the nucleus they adopt. In all cases, however, the energy and spin/parity of the allowed nuclear states following a reaction are of major importance, as it is the states allowed in the presence of various proportions of nuclear matter that are of primary interest to research.

A table is supplied (Table 2), outlining some current models. Not all the models are used in this thesis, but comparing different ways of describing deformation is related to the topic. In the table, Coll. stands for collective, SP for single-particle. CSM refers to Cranked Shell Model, and IBA_1 to the (most general) Interacting Boson Approximation. The SHO is for Simple Harmonic Oscillator, I.T.O. is "in terms of", and R.I. is for Residual Interaction. Single-particle wavefunctions are ψ_i.

Table 2: The major models for deformed, rotating nuclei

Model name	Type	Hamiltonian	Use	I.T.O. other models?	How is R.I. included?
Shell Model	SP	SHO mean field + spin-orbit interaction	Describes the underlying microscopic nucleon distributions for a state. Can extend to excited states of ~7 MeV.	Yes; ψ_i's may be mixed to create Nilsson and CSM states	Included via configuration mixing
Nilsson model	SP	anisotropic oscillator potential	Describing the states of extra-core particles in deformed nuclei	Yes; ψ_i may be expressed in terms of mixed shell-model basis states	Included in part by the use of anisotropic potential
CSM	SP	Shell Model H + Coriolis term		Yes; ψ_i's may be expressed in terms of mixed shell-model basis states	Included via configuration mixing
IBA	SP	$H_{IBA-1} = \epsilon n_d + a_0 P^\dagger \bullet P + a_1 L \bullet L + a_2 Q \bullet Q + a_3 T_3 \bullet T_3 + a_4 T_4 \bullet T_4$	Describing underlying microscopic behaviour in collective nuclei. Can be used to make predictions based on the underlying group theory.	If the s-bosons are ignored, a Hamiltonian similar to the vibrational Hamiltonian results.	Included both as the pairing that creates the bosons, and in the coupling between these.

Continued on Next Page...

Table 2 – Continued

Model name	Type	Hamiltonian	Use	I.T.O. other models?	How is R.I. included?
Particle-Rotor model	Coll.	$H = \sum_{i=1}^{3} \frac{\hbar^2}{2\mathcal{I}_i} I_i^2$	Describing rotational behaviour in nuclei.	No, but orbitals of odd nucleons described by Nilsson model.	Included implicitly in the collective rotation of the core and its coupling to odd nucleons. Causes mixing of orbitals of odd nucleons.
Bohr model	Coll.	$H = T(\beta,\gamma) + U(\beta,\gamma) = \frac{1}{2}\sum_{k=1}^{3} \mathfrak{I}_k \omega_k + \frac{1}{2}B_2(\dot{\beta}^2 + \beta^2\dot{\gamma}^2) + U(\beta,\gamma)$	The background of most current experimental analysis	Tentatively yes	Included implicitly in deformation of nuclear core and its coupling to odd nucleons.
Vibrational model	Coll.	$H_{vibr} = \sum \lambda, \mu \frac{B_\lambda}{2} \lvert \dot{\alpha}_{\lambda\mu} \rvert^2 + \sum_{\lambda\mu} \frac{C_\lambda}{2} \lvert \alpha_{\lambda\mu} \rvert^2$	Describing vibrations in nuclei.	The IBA reduces to a similar Hamiltonian if the s-bosons are not included.	Included via the phonons, since these arise from overlap of orbitals.

3.4 Deformation

Nuclear deformation refers to a deviation from sphericity. As stated, it is the cumulative effect of all the nucleons' distributions, so it is essentially the shape of the many-body potential V (Eqn 3) that dictates nuclear shape. Thus, ground state deformation occurs when N and Z are such that the ground state potential is deformed, dictating distributions that are mixed (shell-model) configurations. Such a potential corresponds to having a large residual interaction.

From a collective (Bohr model) viewpoint, deformation is considered a property of the core. This core includes all the paired nucleons (including paired valence nucleons), and is coupled to any odd nucleons. The shape of the core in turn affects the orbitals of these odd nucleons, deforming them. There is also an argument that interaction with the odd nucleons polarises the core and hence has a hand in its deformation.

For nuclei with larger residual interactions, the first step towards a descriptive single-particle model is to use an anisotropic harmonic oscillator potential for the mean field, as opposed to an isotropic one. This is the approach followed in the Nilsson model [30]. Nilsson model wavefunctions are most generally used for describing the state of the odd nucleon coupled to the core. The Nilsson model is discussed briefly below.

3.4.1 Nilsson Model

The anisotropic harmonic oscillator potential for axial deformation is [26]:

$$v = \frac{1}{2}\mu \left\{ \omega_3^2 x_3^2 + \omega_\perp^2 \left(x_1^2 + x_2^2 \right) \right\}, \tag{4}$$

where the subscripts i = 1-3 indicate in which direction (in a body-fixed co-ordinate system) the distance x_i is measured.

The ω_3 is the oscillator frequency for oscillations along the symmetry axis (the 3-axis), and $\omega_\perp$ is the oscillator frequency perpendicular to the symmetry axis (see Appendix 4). The distortion parameter δ_{osc} is given by [26]:

$$\delta_{osc} = \frac{\omega_\perp - \omega_3}{\omega_0} \tag{5}$$

where ω_0 gives the average oscillatory frequency along all three axes.

This potential (Eqn 4) gives the single-particle Hamiltonian, h [26]:

$$h = \frac{-\hbar}{2\mu}\nabla^2 + \frac{1}{2}\mu\left\{\omega_3^2 x_3^2 + \omega_\perp^2\left(x_1^2 + x_2^2\right)\right\} = t + v. \tag{6}$$

Problematically, this potential extends only to quadrupole deformation, as

$$\begin{aligned} v &= \frac{1}{2}\mu\left\{\omega_3^2 x_3^2 + \omega_\perp^2\left(x_1^2 + x_2^2\right)\right\} \\ &= \frac{1}{2}\hbar\omega_0\rho^2\left(1 - \frac{3}{2}\epsilon P_2\left(\cos(\theta_t)\right)\right), \end{aligned} \tag{7}$$

and $P_2(\cos\theta_t)$ is the Legendre polynomial of order 2. The $\theta_t = \frac{(x^2+y^2)^2}{\rho}$ and ρ is the nuclear radius in spherical co-ordinates.

The solutions to the single-particle Hamiltonian h (Eqn 6) are the Nilsson states. They may be expressed as superpositions of the shell-model states, giving a link between the two models [26]. As the Nilsson states are thus superpositions of eigenstates of the angular momentum operator J, they are themselves not eigenstates of J, necessitating an extra quantum number to completely characterise a state.

The complete list of Nilsson Model quantum numbers is then N, n_3, λ, and Ω. The n_3 counts the number of oscillator quanta along the 3-axis, N gives the energy shell (in units of $\hbar\omega$) at which one finds the orbital in question and Ω

is the projection of the angular momentum onto the 3-axis (see Fig. 4). The additional quantum number λ is given by [26]:

$$\lambda = \pm n_{\perp}, \pm (n_{\perp} - 2), \ldots \pm 1. \tag{8}$$

The odd nucleons may not even occupy a single Nilsson state: more often than not, not even the configuration mixing allowed by the anisotropic harmonic-oscillator is sufficient to express the distributions for these nucleons. Thus, the state is described by a mix of two or more of these states. This gives a rotational band characterised by a linear combination of Nilsson states.

As discussed by [15], a deformed nucleus has rotational degrees of freedom that a spherical nucleus does not, as one can specify an orientation in space for a nonspherical nucleus. Deformation itself may thus be measured via de-excitation from rotational states. Deformation is characterised by several parameters, from several different models. These are discussed briefly below.

Discussing Deformation: Deformation parameters

A selection of the deformation parameters in general use, and their origins, is provided below. The book [30] gives an excellent discussion on these parameters.

δ_{osc}, or ϵ

The Nilsson Model [30] gives us the parameter δ_{osc}, (Eqn 5), which is essentially a measure of how different the oscillator freqencies are for the three different directions of the anisotropic harmonic oscillator. The greater the deformation from the spherical, the greater the value of δ_{osc}. The parameter describes a prolate shape when it is positive, and an oblate shape when it is negative. Note that this parameter is also called ϵ.

ϵ_λ

These also derive from the Nilsson model. As stated, the anisotropic harmonic oscillator potential v only extends to the quadrupole order (se Eqn 7). To extend the model to higher-order deformations, higher-order spherical-harmonics are added to the potential of Eqn 7, as in [30]:

$$v = \frac{1}{2}\hbar\omega\rho^2 \left(1 - \frac{3}{2}\epsilon P_2(\cos(\theta_t)) + 2 \sum_{\lambda=3,4...} \epsilon_\lambda P_\lambda(\cos(\theta_t))\right). \tag{9}$$

The values of ϵ_λ then give the weighting of the higher-order harmonics to which the nucleus is deformed, via the direct interplay between the shape of the potential and that of the nucleus itself.

β and γ

Deformation is most easily expressed via the shape of the nuclear surface, which is parameterised as in Eqn 1. From this parameterisation, we have the parameters $\alpha_{\lambda\mu}$, which are the amplitudes of the different orders of deformation for the nuclear surface. Their magnitude is thus an indicator of deformation type and extent. With λ set to equal two, we derive the (Lund convention) deformation parameters β and γ [26]. These are used in conjunction with the rotational model, and in the Bohr model, where they are used to determine the mass and elasticity parameters. As $\lambda = 2$, they *only* apply to quadrupole deformation. They are expressed as [16]:

$$\begin{aligned} \alpha_{20} &= \beta\cos\gamma \\ \alpha_{22} = \alpha_{2-2} &= \beta\sin\gamma \end{aligned} \tag{10}$$

so that the parameter β expresses the eccentricity of the ellipsoidal shape [27]. Its sign changes depending on the nature of the deformation (positive for prolate shapes; negative for oblate shapes) [27]. The parameter γ gives the level of triaxiality: that is, whether the shape is axially symmetric about some axis or not. In this convention, the (positive) value γ must generally be $\neq 0°$ for there to be components $\alpha_{\lambda\mu}$ with $\mu \neq 0$ (Eqn 11). Thus, when γ is $\neq 0°$, there is asymmetry, as $\mu \neq 0$ for the shape in question.

There are other ways of deriving these parameters, which relate them to the frequencies ω_{1-3}; and there are other conventions for the values of of γ and β for shape and triaxiality [30]. In the Lund convention, the value $\gamma = 0°$ (and even multiples of 60°) gives prolate shapes, $\gamma = 60°$ (and odd multiples of 60°) gives oblate shapes, while any value of γ in between these gives triaxially-deformed shapes [16]. The value of β is quadratically-related to the intrinsic quadrupole moment Q_0 [27].

These parameters (β and γ) are very important, as they are used as the internal degrees of freedom in both the rotational model and the Bohr model [16]. Unfortunately the parameters are solely for quadratic deformation, as the dependence of the Bohr and rotational models on these then means the models are only geared towards nuclei that are quadrupole-deformed.

Q_0 and Q_A

These two parameters are the intrinsic and observed quadrupole moments respectively. The Q_0 is the quadrupole moment operator, and Q_A is the expectation value for that operator when evaluated between the states coupling to the angular momentum of the overall state.

3.5 Rotation

Rotation refers to a periodic change in the angular distribution of the nucleon density. Such rotation can only occur in a deformed nucleus, as its potential is anisotropic with respect to angle, and so its nucleon-distribution has an angular-dependence. In a nucleus with a spherically-symmetric potential, no variation in the probability density with angle is detectable. Nuclear rotation thus results as much from an anisotropic potential as from the angular momentum transferred by the collision.

The nuclear core rotates with angular momentum **R**. Within the core, all the nucleons are paired, and the angular momentum **R** of the core is completely collective. The core rotation is coupled to that of the odd nucleons, and the angular momentum of these odd nucleons is referred to as **J**; the nuclear spin. An even-even nucleus will therefore have $\mathbf{J}=0$. These angular momenta are coupled in one of the two ways mentioned previously (Section 2.1): DAL or RAL coupling. The total angular momentum of the nucleus is $\mathbf{I} = \mathbf{J} + \mathbf{R}$.

For a rotating nucleus, the system wavefunction Ψ has two parts: an intrinsic part, Φ, encoding the radial distribution of the core and the configuration of the odd nucleons, and a rotational part, Θ, which contains the information about the angular distribution. This structure of Ψ is why it is possible to speak of a rotational band: a "ladder" of states of increasing I, all based on the same deformation. In a band, the rotational part (Θ) changes, but the intrinsic wavefunction (Φ) stays the same. As the configuration of the odd nucleons does not change, J remains of equal magnitude for a band, and only R (the angular momentum of the core) alters, bringing about a change in I.

The intrinsic and rotational wavefunctions are usually derived using the Particle-Rotor (PR) model. This is discussed briefly below.

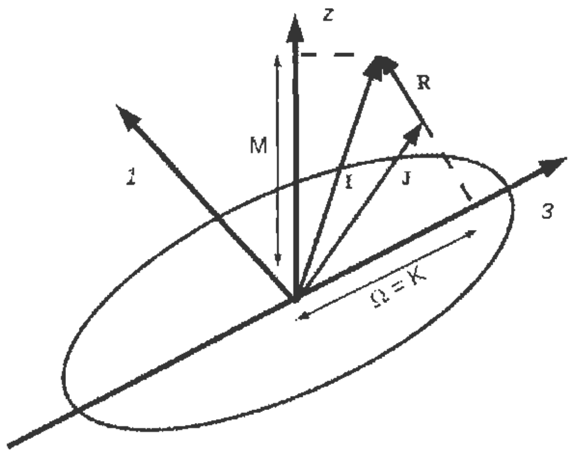

Figure 4: Angular momenta and axes in the rotational model. The body-fixed axes are labelled with numbers $1-3$; the laboratory frame with $x-z$. The angular momenta **J** and **I** are in the body-fixed and laboratory frames, respectively. **R** is the rotational angular momentum [32].

3.5.1 Particle-Rotor model

In this model the nucleus is considered in two reference frames: a rotating (body-fixed) frame, in which the nucleus posesses some **J** but is not rotating with **R**, and the (non-rotating) laboratory frame, in which the nucleus and the body-fixed frame rotate with angular momentum **R** (Fig. 4). Each reference frame has its own set of axes. The body-fixed frame is such that the 3-axis is the symmetry axis of the core.

The projections of the three angular momenta (**I**, **J** and **R**) provide the three quantum numbers needed to specify the state of the rotating body. They are: M, the projection of $\vec{I}$ on the z-axis; K, its projection on the 3-axis, and Ω, which is the projection of **J** on the 3-axis (see Fig. 4). The values Ω and K are equal where **R** is perpendicular to **J** [32]. Since **J** remains constant for a single band (and **J** and **R** are usually perpendicular), the value of K is also normally constant for a band. Thus, bands are usually referred to by their K-value.

The Hamiltonian for the PR model is given by [26]:

$$H = \sum_{i=1}^{3} \frac{\hbar^2}{2\mathcal{I}_i} I_i^2, \tag{11}$$

where I_i indicates the angular momentum along the (body-fixed)axis i and $\mathcal{I}_i$ is the rotational moment of inertia of the nucleus along that axis. This equation simplifies to [26]:

$$H = \frac{\hbar^2}{2\mathcal{I}}(I^2 - I_3^2) + \frac{\hbar^2}{2\mathcal{I}_3} I_3^2 \tag{12}$$

for an axially-symmetric nucleus.

When the angular momentum of the nucleus increases, the energy associated with the rotational part increases. The energy increments between successive states in a rotational band are given by [26]:

$$E = \frac{\hbar^2}{2\mathcal{I}} I(I+1) + E_K = A(I(I+1)) + E_K \tag{13}$$

It is these "steps" in energy of $I(I+1)$ which are characteristic of pure rotational bands. The offset E_K is zero for $K = 0$, and increases for increasing K. It dictates the band-head energy, and represents contributions from the intrinsic wavefunction [26].

The lowest value of I for a band will be $I = K$ if the rotation is taking place around the x-axis, which is most often the case. Thereafter, as more rotational kinetic energy is added to the system, $I = K+1, K+2...$ *etc.* [26]. The K-value of the band must be known for one to be able to transform from the laboratory frame to the intrinsic frame, where concepts like rotational frequency ω can be defined [28]. A $K^{\pi} = 0^{+}$ band will only feature states of even I, due to symmetry requirements [28].

The moment of inertia $\mathcal{I}$ of the system (Eqn. 12-13) changes with higher rotational angular momentum, as that of a liquid drop would [27]. Usually, the nuclear moment of inertia $\mathcal{I}(I, \omega)$ increases quadratically as rotational frequency increases (rearrangement of Eqn. 14), giving a linear plot of $I, \omega)$ with ω^2. However, a sudden decrease of $\mathcal{I}$ in these plots is sometimes observed; referred to as“backbending” as the plot bends back on itself. This is considered indicative of Coriolis alignment of the odd-nucleon orbitals [33] (a change in the configuration of the odd nucleons) or, equally, of band-crossing with another band (with a different $\mathcal{I}$), close in energy to the first [26]. These are equivalent, since a change in alignment would cause a change in the overall intrinsic state and $\mathcal{I}$, and thus a change from one band to another. The two bands will have different K values, since the states of the odd nucleons are different.

It must be stated that the term “moment of inertia” is often used loosely to describe any one of the following three quantities: the static moment of inertia $\mathcal{I}$, the kinematic moment of inertia $\mathcal{I}^{(1)} = \frac{I}{\omega}$, and the dynamic moment of inertia $\mathcal{I}^{(2)} = \frac{dI}{d\omega}$ [28]. It is the static moment of inertia $\mathcal{I}$ which is referred to above and in Eqns 13-14.

Note that K is not a good quantum number for triaxially-deformed nuclei. In these nuclei, a single rotational band may not necessarily be an eigenstate of the rotor Hamiltonian, and so a single state is described by a superposition of states of different K [16]. Secondly, for triaxially-deformed nuclei there is also no single well-defined axis of rotation. This allows for non-identical states with the same K-values, making K a poor quantum number [16]. Any additional perturbation of the Hamiltonian (Eqn. 12) will necessarily mix rotor eigenstates [34] and thus make K a poor quantum number.

It is interesting to consider the mixing of wavefunctions and how this relates to rotation: In the ground state, all orientations of the core are equally probable. Thus, the nucleus is in a superposition of all possible orientations of the ground state wavefunction, all equally weighted. Therefore, if one has just a core (*i.e.* no unpaired nucleons) a 0^+ ground state exists, even though the basis wavefunctions may be for a deformed potential. When energy is added to the system, the potential V changes, and there is directional preference introduced [35]. Thus, spatial orientations are no longer equally favourable, and some are weighted over others, making deformation evident.

3.6 Vibration

Nuclear vibration refers to periodic alterations of the nuclear shape through variation of the radial distribuion of the nucleons [16]. Such vibrations come about due to the mixing of two equally weighted single-particle states, both of which are accessible to a large number of nucleons. These nucleons oscillate from one state to another, which results in an overall oscillation from one macroscopic state to another. This is discussed in various phase approximations like TDA or RPA [25].

The multipolarity of the residual interaction itself dictates which configurations it will mix (*e.g.* a dipole interaction would mix states differing in angular momentum by one unit). Thus, this dictates the nature of the vibrations [4]. The kinds of vibration possible at different energies are therefore an important window onto the internucleon interactions at those energies.

Rather than a microscopic view on vibrations, a macroscopic one is generally followed, using the concept of "phonons" from solid-state physics, which avoids introducing a time-dependence into the system Hamiltonian (Eqn. 2). The phonon is itself the energy involved in the oscillation: the difference between the energies of the overall nuclear states between which the vibrations take place. The phonon has multipolarity λ dependent on the difference in angular momentum i between the mixed valence states, that is: $\lambda = |i_i - i_f|$ [27]. A difference of 3 units of i would therefore give rise to an octupole vibrational phonon. The phonon is created via the mixing: the motion of the particles changes the electric and magnetic fields around the nucleus and thereby gives rise to electromagnetic radiation.

Vibrations will tend to occur in nuclei in which the residual interaction is intermediate in strength: it is strong enough to mix certain configurations and make excitation between them collective, but it is not so strong that collective rotation may take place.

A nucleus can possess more than one phonon of a certain order, depending on the different orientations of the oscillations. However, more than one phonon brings with it the problem of coupling. Being bosons, phonons must always be coupled such that their wavefunction is totally symmetric [25], and this limits the overall J of the nucleus arising when two or more nuclear vibrations are coupled. The most commonly-occuring multi-phonon states are: two quadrupole phonons (giving allowed I-values of 0^+, 2^+, and 4^+), and three quadrupole phonons, (which gives allowed I-values of 0^+, 2^+, 3^+, 4^+ and 6^+). The allowed values are obtained via combining m-values for the phonons in the allowed ways [25].

The Interacting Boson Approximation (IBA) considers vibrations as arising from a coupling of valence nucleons into a boson of certain total angular momentum. The angular momentum of the odd boson will then dictate the angular momentum associated with the vibration: *e.g.* an odd $\lambda = 2$ boson (a d-boson) will be associated with a quadrupole vibration [25]. The coupling of two quasi-particles into a boson is equivalent to the coupling of states that gives rise to a phonon.

Vibrations are also classified according to along which axes they occur. Radial oscillations of the matter-distribution can either occur along two axes at the same rate (maintaining a spherical cross-section); or they may occur at different rates in all three directions, in which case a spherical cross-section is not maintained [26]. The first (β-vibration) is indicative of a potential which changes in a way symmetric about the long-axis; while the second (γ-vibration) indicates that the potential is changing anisotropically: a case that can only arise if the initial distribution was somehow anisotropic. Thus, γ-vibrations only occur starting from an already-deformed shape: that is, between states which are permanentely deformed [26].

3.6.1 Vibrational Hamiltonian

The approach most generally followed for describing collective motions is to use the Rotor Hamiltonian (Eqn 12) for rotation, and the vibrational part of the Bohr Hamiltonian for vibrations.

Thus, the Hamiltonian used for vibrations is [16]:

$$H_{vibr} = \sum_{\lambda\mu} \frac{B_\lambda}{2} |\dot{\alpha}_{\lambda\mu}|^2 + \sum_{\lambda\mu} \frac{C_\lambda}{2} |\alpha_{\lambda\mu}|^2 \tag{14}$$

where B_λ is the "inertial parameter" for the nucleus with multipole moment λ, and C_λ is analogous to the "stiffness" that defines a restoring-force for a spring [16]. This Hamiltonian essentially uses the parameterisation of nuclear shape that the Bohr model supplies, but gives it a time-dependence. It may be re-written in terms of phonon creation and annihilation operators as [16]:

$$H_{vibr} = \sum_{\lambda} \hbar\omega_{\lambda} \sum_{\mu} (b^{+}_{\lambda\mu} b_{\lambda\mu} + \frac{1}{2}) \tag{15}$$

where the frequencies ω_{λ} are those of the oscillation, and $b^{+}_{\lambda\mu}$ and $b_{\lambda\mu}$ are the phonon creation and annihilation operators, respectively.

Oscillations in distribution along two axes are equivalent to a rotation (except in the case of isotropic oscillations), so rotational angular momentum is imparted to the nucleus through vibrations. The amount of rotational angular momentum imparted is given by the multipolarity of the phonon involved and in the case of more than one phonon it may be determined by coupling the phonons [27].

It must also be mentioned that a vibrational state may also rotate: the two behaviours may happen at once. Such a vibrational band will have the characteristics of a rotational band, but appear as two distinct structures, one with even spin and one with odd spin (these two bands may also have opposite parity).

3.7 De-excitation, transitions and signatures

Interaction with some outside influence (*e.g.* during a collision) will alter the nuclear potential V, and introduce a time-dependence into the Hamiltonian, *i.e.* [27]:

$$H = H_0 + H(t) \tag{16}$$

Oscillation of the system will cause changes in the surrounding electromagnetic field, causing a radiation field to be set up. This may possess angular momentum, the value of which derives from the moment of the field. This boils down to the field quanta–the photons–having a characteristic angular momentum λ. Thus, photon angular momentum is directly dependent on the nuclear shape [27]. It is this dependence which makes γ-rays of great importance in elucidating nuclear structure.

The time-dependent part of the Hamiltonian (Eqn 16) may be expressed in terms of the electromagnetic transition operators $O_{\lambda\mu}(E\lambda)$ and $O_{\lambda\mu}(M\lambda)$ [26]:

$$\begin{gathered} O_{\lambda\mu}(E\lambda) = \textstyle\sum_{i=1}^{A} e(i) r_i^{\lambda} Y_{\lambda\mu}(\theta_i\phi_i) \\ O_{\lambda\mu}(M\lambda) = \sqrt{\lambda(2\lambda+1)} \textstyle\sum_{i=1}^{A} r_i^{\lambda-1} \\ \left\{ \left(g_s(i) + 2\tfrac{g_l(i)}{\lambda+1} \right) \left(Y_{\lambda+1}(\theta_i\phi_i) \times \mathrm{s}_i \right)_{\lambda\mu} + \tfrac{2g_l(i)}{\lambda+1} \left(Y_{\lambda-1}(\theta_i\phi_i) \times \mathbf{j}_i \right)_{\lambda\mu} \right\} \qquad (17) \end{gathered}$$

where the operators $g_s(i)$, $g_l(i)$ and $e(i)$ act to give the spin, angular momentum and charge of particle i, and $\mathbf{j}_i = \mathbf{l}_i + \mathrm{s}_i$. The operators $O_{\lambda\mu}(E\lambda)$ and $O_{\lambda\mu}(M\lambda)$ are proportional to photon creation operators, and so create photons $E\lambda$ or $M\lambda$ in character respectively.

The angular momentum λ and polarisation (that is, electric or magnetic character) of transitions may be determined via measuring their angular distribution and scattering behaviour (Section 4.5).

The properties of the operators $O_{\lambda\mu}$ reflect characteristics of electric and magnetic transitions, notably their probabilities and their ability to change parity of a state (the parity of a nuclear state being linked to its overall angular momentum I and the symmetries of its shape). The parity and probability rules for various transitions are discussed briefly below.

Parity and Angular Momentum rules

The angular-momentum λ of a transition is related to the angular momenta of the states it links by the equation [27]:

$$\mathbf{I}_i = \lambda + \mathbf{I}_f \tag{18}$$

for any transition (where one considers the transition as a de-excitation; so $\mathbf{I}_i > \mathbf{I}_f$). As a result of this relationship, the angular-momentum selection rule for transitions is [27]:

$$|\mathbf{I}_i - \mathbf{I}_f| \geq \lambda \geq |\mathbf{I}_i + \mathbf{I}_f|. \tag{19}$$

There may be more than one value of λ which solves this vector sum (Eqn 18), so few transitions have a single angular momentum λ. The degree of mixing depends mainly on the probabilities of the possible transitions, as dictated by their λ and their electric or magnetic character. Transitions with λ greater than 3 are generally ignored because of their low probability. Mixing is expressed via the mixing ratio δ [26]:

$$\delta^2 = \frac{W(E(\lambda + 1))}{W(M(\lambda))}, \tag{20}$$

when $E(\lambda+1)$ refers to the electric part and $M(\lambda)$ to the magnetic part, in the case of the electric component E having a higher multipolarity than the magnetic component M. This is usually the case due to energy-considerations: magnetic transitions in general are unable to compete with electric because of the higher energies involved in causing them.

It is impossible to create a photon with an angular momentum of zero (since it has spin 1), but x-rays may be observed associated with an $|\mathbf{I}_i - \mathbf{I}_f| = 0$ transition, as a result of internal conversion. As a state decays, the ensuing change in the nuclear electromagnetic field may affect the surrounding electrons, causing an electron to be emitted from its orbit. A neighbouring electron de-excites into the gap, so a photon is given off, despite there being no associated change in the angular momentum of the nucleus [28]. The $E0$ transitions observed are more properly x-rays resulting from internal conversion.

In the case where the angular momentum of the transition is greater in magnitude than $|\mathbf{I}_i| - |\mathbf{I}_f|$, the transition is referred to as "unstretched", as, figuratively, its angular momentum vector is greater than the "gap" in angular momentum, $|\mathbf{I}_i| - |\mathbf{I}_f|$.

The parity rules for electromagnetic transitions are dictated by the dependence of the transition operators $O_{\lambda\mu}$ on the spherical harmonics $Y_{\lambda\mu}(\theta, \phi)$ (Eqn 17) [26]. As $O_{\lambda\mu}(E\lambda) \propto Y_{\lambda\mu}$, then $O_{\lambda\mu}(E\lambda) \rightarrow (-1)^{\lambda} O_{\lambda\mu}(E\lambda)$ with reflection, so an even-λ stretched electric transition causes no change in parity between levels. As $O_{\lambda\mu}(M\lambda) \propto r^{\lambda} Y_{\lambda\mu}$, then $O_{\lambda\mu}(M\lambda) \rightarrow (-1)^{\lambda+1} O_{\lambda\mu}(M\lambda)$ on reflection, so odd-λ stretched magnetic transitions preserve level parity. Conversely, then, odd-λ electric transitions and even-λ magnetic transitions will connect states of opposite parity [27], in the case of stretched transitions. The opposite is true for unstretched transitions: even-λ unstretched electric transitions will link states of opposite parity *etc.*.

Transition probabilities

The probability of any transition ($W(\lambda)$) is, naturally, proportional to the expectation values of the operators $O_{\lambda\mu}$ (Eqn 17). In general, magnetic transitions are less probable than electric transitions of the same order [26]. Magnetic transitions require a change in the current distribution as well as in the charge distribution, hence the inclusion of the ∇ in the transition operator $O_{\lambda\mu}(M\lambda)$ which greatly reduces its expectation value compared to

$O_{\lambda\mu}(E\lambda)$ (See Eq. 17). The electric transitions are thus (usually) far more probable [26].

Also, [26]:

$$\frac{W(\lambda+1)}{W(\lambda)} \sim (kr^2) \tag{21}$$

where k and r are the magnitude of the wavenumber for the transition and r is the distance of the point from the centre of the electromagnetic field, respectively. According to this relation (Eqn 20), when comparing transitions of the same type, (both electric or both magnetic), the lower-λ transitions are considerably more probable. This is why (electric) octupole transitions are only occasionally considered, and higher-order transitions not at all.

The transition rates, or probabilities, are most often given in Weisskopf units (W.u.); where one Weisskopf unit is equivalent to the probability of a single proton making the transition from one shell-model state to another [27].

Band signatures

While "signature" refers to a particular quantity [16], one often refers to those qualities observed in a band which indicate the underlying structure as "signatures". Some of these are discussed below.

The nature of intra-band transitions is especially characteristic of nuclear shape, due to the link between the multipolarity and photon angular momentum. A band based on a structure with no quadrupole component in its shape (*e.g.* a tetrahedral shape) would, for example, not undergo electric quadrupole transitions, as the oscillation of its charge would not set up an electric quadrupole field [20].

The energy of transitions between levels (E_γ) is another good indicator of nuclear behaviour: $E_\gamma \propto I(I+1)$ is characteristic of pure rotor behaviour, and thus of static deformation (Eqn 13). If it possesses them, a ratio of the energies of the 2_1^+ and 4_1^+ levels of a band ($E_{\gamma 4+}/E_{\gamma 2+}$), evaluating to ≈ 2 would indicate a quadrupole vibrational band, while one of ≈ 3.33 indicates a pure rotational band [25].

The band-head energy is reflective of internal structure: the more low-lying the band, the more accessible the orbitals which contribute to the structure. Thus, bands with low band-head energies are indicative of shell closure of some kind, as the occupied levels must be lowered in energy, creating an energy gap above them [5]. Also, the lower the band-head energy, the more collective the structure is, since low energy indicates that the contributing orbitals are accessible to a large number of nucleons.

The lifetime of a state is naturally reflected in the probability of the transition from that state [36]. The lifetime is also indicative of intrinsic structure, since metastable states have a very different intrinsic structure to that of the available lower states.

3.8 Tetrahedral states and the model for octupole deformation

While some signatures of static octupole deformation have been observed (notably in ^{128,129}Ba and ^{190}Hg [9,36]), experimental documentation of such states is still fairly minimal. However, structures similar to octupole vibrational bands, but with no intra-band $E2$ transitions, were documented in (among others) ^{160}Yb, ^{154,156}Gd, ^{152}Sm and $^{230-234}$U [21], and led to the postulation of static tetrahedral deformation (a subtype of octupole deformation) [2]. The tetrahedral model was thus originally formulated to describe these bands, which proved otherwise rather difficult to explain [2].

In parameterisation (Eqn 1) of a tetrahedrally-shaped nucleus, only odd-λ $\alpha_{\lambda\mu}$ values will be nonzero. Of these odd $\alpha_{\lambda\mu}$s, all will have negligible values, except for α_{32}, which itself will have limited values [38].

The tetrahedral nuclear shape is described as "pyramidlike, with rounded edges and corners" [2], as in Fig. 5, below. Signatures for tetrahedral deformation are known from theory [1,21], but tetrahedrally-deformed nuclei have not been identified conclusively in experiment to date: closer studies of some of the nuclei listed above have indicated that there may be very low-intensity $E2$ intra-band transitions in the proposed tetrahedral bands, ruling out the tetrahedral nature [12].

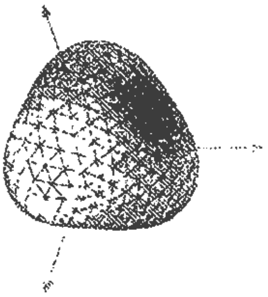

Figure 5: The shape of a tetrahedrally-deformed nucleus [1].

The model

The idea behind the tetrahedral model is the well-known principle that the symmetry of the nuclear potential directly dictates the symmetry of the nuclear shape [18]. With this in mind, this model is based on extending existing

Hamiltonians (both macro- and microscopic) to have symmetry groups pertinent to octupole deformation: the groups O_h^D and T_d^D, respectively (where the D denotes an addition to the groups O_h and T_d to make them applicable to fermionic systems [1]).

The procedure followed is, essentially, to determine additions to the Hamiltonian in question such that it satisfies the equation [1]:

$$\hat{g}_i H = H \tag{22}$$

where $\hat{g}_i$ are the symmetry operations for the group under which H is to be symmetric (O_h^D or T_d^D for the octupole and tetrahedral cases, respectively).

How this constraint (Eqn 22) is implemented in various models depends on how information about the nuclear shape feeds into the model. In the Woods-Saxon potential V_{WS}, where the shape enters via dependence on the distance from the nuclear surface $dist\Sigma$ or, [38]:

$$V_{WS} = \frac{V_0}{l - e^{dist\Sigma}}, \tag{23}$$

the condition (Eqn 22) becomes [38]:

$$\sum_{\lambda=2}^{\lambda_{max}} \sum_{\mu=-\lambda}^{\lambda} \alpha_{\lambda\mu}(g_I Y(\theta, \phi)) = \sum_{\lambda=2}^{\lambda_{max}} \sum_{\mu=-\lambda}^{\lambda} \alpha_{\lambda\mu}(Y_{\lambda\mu})(\theta, \phi), \tag{24}$$

where g_i are the symmetry operations of the group which one requires as the symmetry group of H.

The values of $\alpha_{\lambda\mu}$ that satisfy Eqn 24 will parameterise the nuclear shape such that it has closure under the symmetry group in question [1]. Some values determined in this manner for tetrahedral deformation are supplied in the table below (Table 3), where the t_i values are constants to be determined via applications to particular nuclei [1].

Table 3: The first six parameters $\alpha_{\lambda\mu}$ for tetrahedral deformation (from [1]).

parameter	value
$\alpha_{3,\pm2}$	t_3
$\alpha_{5,\mu}$	no solution
$\alpha_{7,\pm2}$	t_7
$\alpha_{7,\pm6}$	$-\sqrt{\frac{11}{13}}t_7$
$\alpha_{9,\pm2}$	t_9
$\alpha_{9,\pm6}$	$\sqrt{\frac{28}{198}}t_9$

The same equation (Eqn 24) holds for other single-particle methods, such as the Hartree-Fock-Bogoliubov method, where $\alpha_{\lambda\mu}$ is replaced with the multipole-moment constraint $Q_{\lambda\mu}$ [1]. In the case of the macroscopic Particle-Rotor Hamiltonian, a tensor operator $h(\{p\}\, I_x, I_y, I_z)$ is found such that the Hamiltonian (Eqn 13) satisfies the required condition (Eqn 22) [1]. The process is detailed in [20].

If the tetrahedral model were to be verified, then not only would a very useful method for predicting deformations be shown as correct, but an accurate description of the seemingly-vanishing $E2$ transitions in, for example, the lowest-lying negative-parity bands of $^{230-234}$U, would have been reached [21].

Discovery of tetrahedral bands would also ask the question: why would nuclei take on such a deformation? Would it be evidence of a particularly powerful octupole component to the residual interaction when certain orbitals are occupied?

One may also question what the predictions mean physically. Would the tetrahedral shape necessarily be static; or would the nucleus express such a symmetry, but not necessarily sustain it statically? That is, would "tetrahedrally-magic" nuclei vibrate to a tetrahedral shape in some octupole vibration, rather than being statically tetrahedral?

How a static tetrahedral structure would come about physically is another consideration: A structure consisting of α-particles packed into a tetrahedron has been considered. If this is so, then would there need to be some sort of combination of magic numbers involved: one that would give a tetrahedral number[2] of α-particles? These are all questions worth considering in the light of any possible affirmative results.

Tetrahedral "magic numbers"

The tetrahedral magic numbers have been determined via the appplication of the parameterised Woods-Saxon potential (Eqn 24) to various values of N and Z [2]. The values of the t_λ parameters (see Table 3) were varied, and energy-minima observed with different N and Z. The value t_3 is as in Table 3, so that $\alpha_{32} = t_3$. The magic numbers thus determined are [2]:
N = 16, 20, 32, 40, 56, 70, 90, 112, 136
Z = 16, 20, 32, 40, 56, 70, 90, 112, 126.

Studies have already been undertaken exploring the possibility of static tetrahedral shapes at the magic numbers $Z = 70$, $N = 90$ (^{160}Yb) [12], but no bands with the required decay signature were conclusively observed.

---

[2] Here, a "tetrahedral number" is a number of objects that will pack into a tetrahedral shape: *e.g.* 4, 10... $\frac{n(n+1)(n+2)}{6}$ for integer $n > 1$.

Signatures of Tetrahedral states

Strictly speaking, nuclei of static tetrahedral shape would have no dipole or quadrupole moment (only the parameter α_{32} is appreciably different from 0, so no dipole or quadrupole fields result from the charge-distribution) [20]. Despite this, intra-band $E1$-transitions are expected to arise from dipole zero-point motions around the tetrahedral shape [20]. Thus, the most important characteristic of tetrahedral bands is a complete absence of intra-band $E2$ transitions (although it has been suggested that quadrupole zero-point motions give rise to very low-intensity $E2$s for tetrahedral nuclei of certain A [20]).

Secondly, tetrahedral bands will be low-lying; the tetrahedral shape being particularly accessible and energy-minimising for the nuclei in question [20]. Due to this energetically-favourable nature, tetrahedral isomers may also be particularly long-lived. All the levels in the tetrahedral band will be of negative parity, because of the $\lambda = 3$ nature of the structure [20].

Since ^{72}Ge is a strongly vibrational nucleus, and the $E2$ transitions are enhanced by the lowering in energy of the $g_{\frac{9}{2}}$ orbital [8], the likelihood of observing a structure with no $E2$ transitions seems small. However, the low-lying $g_{\frac{9}{2}}$ orbitals will also tend to make octupole phenomena strongly collective, perhaps even static [3], so the possibility of a static tetrahedral state cannot be ruled out for ^{72}Ge by these considerations alone.

4 Experimental Procedures

4.1 Outline of Procedure

Data-generation was fairly standard: the nucleus of interest was produced in a fusion-evaporation reaction with a large-enough cross-section to produce good statistics. Only coincident γ-rays were recorded.
Sorting, calibrating and classification procedures used in this experiment are discussed below, along with relevant background on detectors and equipment (Section 4.2-4.4).

4.2 Particulars of the reaction

The experiment (PR152[3], November 2008) took place at iThemba LABS, Somerset West, using their resident detector array (AFRODITE) and K=200 separated-sector cyclotron. The fusion-evaporation reaction used in this experiment was

$$^{70}\mathrm{Zn} + \alpha \rightarrow ^{72}\mathrm{Ge} + 2\mathrm{n}. \tag{25}$$

This was chosen because it was determined in the original study [10] that the evaporation of two neutrons means the reaction (Eqn 24) represents 90% of the cross section, as opposed to the possible p-n or $2p$ reactions, which gave a much lower yield of ^{72}Ge. The α-particles had an energy of 30 MeV, which was also recommended by [10] for maximum yield.

The target was a zinc sheet of thickness 0.5 g.cm^{-2}, which is sufficient to stop recoiling nuclei.

---

[3] Collaborators were: D. G. Roux, R. A. Bark, S.P. Bvumbi, E. A. Gueorguieva-Lawrie, J. J. Lawrie, T.E. Madiba, S. M. Mullins, S.H.T. Murray S.S. Ntshangase, L.P. Masiteng and O. Shirinda

4.3 Detectors and detector array

Detectors for γ-ray spectroscopy consist, essentially, of one or more crystals of semiconductor material. A γ-ray colliding with the detector will excite a number of electrons N, where N is proportional to the energy supplied by the γ-ray, across the band-gap. This liberated charge is collected by an applied potential difference and recorded as a voltage-pulse, the height of which is thus proportional to the energy of the γ-ray.

The semiconductor crystal (most often germanium, because it is possible to produce very large single Ge crystals with high purity [39]), is surrounded by a Compton-suppression shield, for recording transitions which scatter out of the detector, and a flask of coolant (usually liquid nitrogen) (see Fig. 6). The attached electronics used for recording events is illustrated in Fig. 9 (Section 4.4).

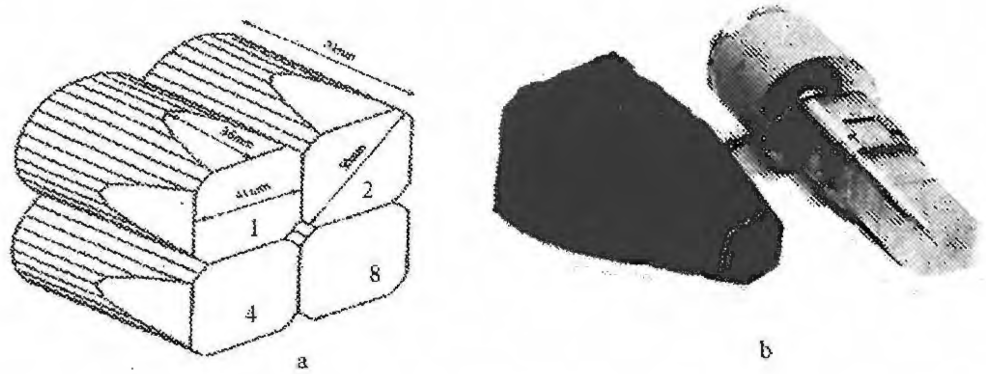

Figure 6: The four Ge crystals or elements in a Clover detector (Fig. 6a). The number on each Clover element is the value of the associated bit pattern [40]. Figure 6(b) shows a Clover detector and its escape-suppression shield [41].

The detectors used in this experiment were all Clover detectors. These detectors consist of four discrete Ge crystals (Fig. 6), for indicating scattering direction (see Section 4.5.2). For this experiment, the array at iThemba consisted of 9 Clovers, arranged as in the diagram below (Fig. 7). The polar angle θ is either 135° or 90°, as shown. The azimuthal angle for each detector placement is indicated.

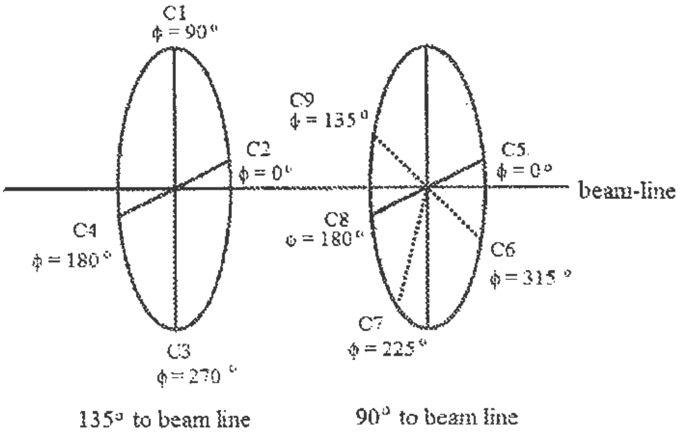

Figure 7: A schematic diagram of the detector array, showing positioning of the 9 Clover detectors (C1-C9). In actuality, both rings shown would be superimposed (with one 45^o to the other) and the target would lie in their centre.

In this configuration, the average azimuthal angle of separation ($\Delta\phi$) for detectors at $\theta = 135°$ is $\Delta\phi = 45°$, and for detectors at $\theta = 90°$ it is $\Delta\phi = 27°$. For pairs with one detector at $\theta = 135°$ and the other at $\theta = 90°$, $\Delta\phi = 45°$. These average angles were calculated by summing over all possible pairs, taking into account that the angular distributions are symmetric around 90° (back- and forward-angles are equivalent), and symmetric with respect to ϕ. These average $\Delta\phi$ values were used in all calculations of angular distribution.

The orientation of each detector with respect to the beam direction is shown in Fig. 8: each detector was oriented so that elements of bit-value "1" and "2" lay closest to the beam direction. Having a known detector orientation allows determination of scattering-direction from the bit pattern (Section 4.5.2.).

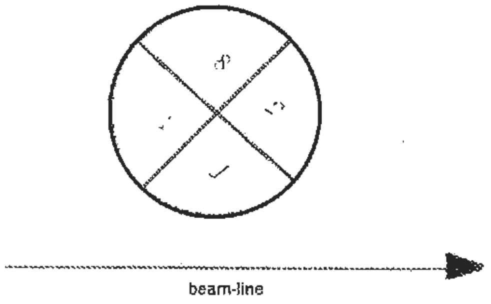

Figure 8: Orientation of the individual Clover detectors with respect to beam line. Numbers on the four elements indicate the bit-values.

4.4 Data Collection and Analysis

The data were recorded via a system of electronics similar to that illustrated schematically in Fig. 9 [42]. A coincidence-window of 150 ns was used. The master gate demanded a coincidence between at least 2 of the 9 Clovers and the radio-frequency signal generated by the cyclotron when the beam pulse arrives at then target. Thus the minimum fold of events in the data set was 2.

After collection, data were sorted into various data-structures for use in creating the level scheme. The data-sorting and data-structures are discussed in Section 4.4.1. Additional corrections are discussed in Section 4.4.2.

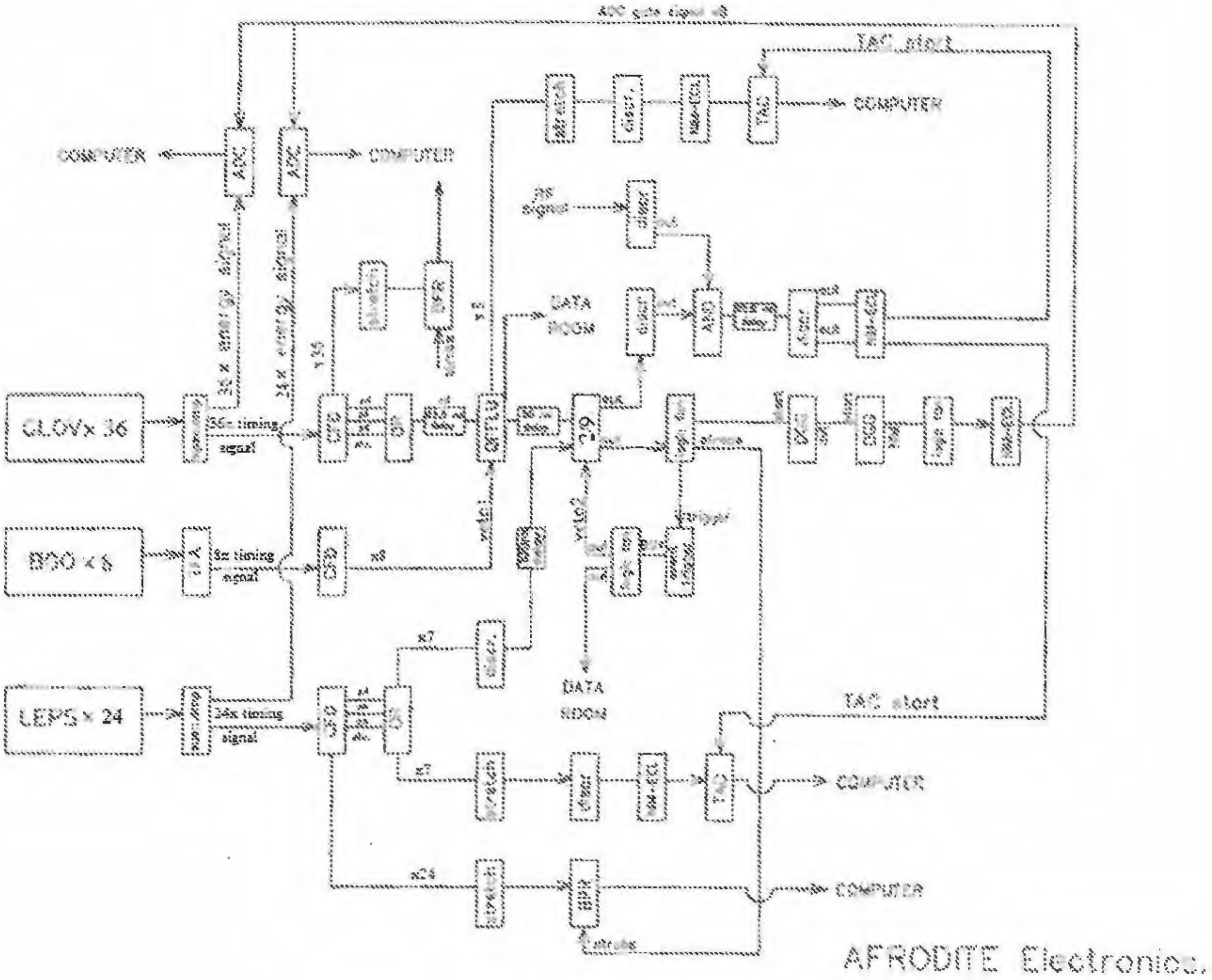

Figure 9: A schematic general diagram of the electronics for data-recording [42]. The data are recorded as coincidence events via the comparison of signals from each detector.

4.4.1 Sorting and data structures

The coincidence events were sorted into two kinds of structure: one recording the intensity of each γ-γ coincidence (γ-γ matrix), and others recording intensity of coincidences between detectors placed at different angles θ relative to the beam. The latter are discussed more in Section 4.5.

The data-structures are in essence two- or higher-dimensional arrays, in which each position or "bin" in the array is incremented for a particular coincidence (see Appendix 1 for a brief elucidation). Thus they function as histograms with two (or more) criteria for each bin.

In this analysis, two-dimensional histograms were used for both structure-types. A three-dimensional histogram was also made for recording regularity of coincidence, as there were several very complicated coincidence relationships encountered.

The data-structures produced for this experiment are listed in Table 4.

Table 4: Data-structures used in sorting.

Structure type	
Symmetric	Asymmetric
time-gated γ-γ matrix	time-gated DCO-matrix (90-135)
γ-γ-γ cube	Polarisation matrix

The sorting was all performed after recording, via the sorting-program MTSort [43] (see Appendix 1 for a brief overview of the sorting process).

The use of the structures in level scheme production was facilitated by *escl8r* [44], a program which allows gating on the matrix. Naturally, the success of spectra in level scheme building depends on the resolution of the data, and this varies for different experiments. For this experiment, the FWHM at 1 MeV was $\sim$ 2.8 keV, giving an energy resolution $R = 0.28\%$ at this energy.

During sorting, additional corrections were performed to override various errors and processes which occur during recording. These are detailed briefly below.

The "addback" of recorded energies, (required to account for scattering of the γ-ray between elements) was performed via MTSort. The two recorded energies from a single scattered γ-ray (recognised by the detector bit pattern) are added together, so it is correctly recorded as a single transition. Gain-drift correction (Appendix 2) was also implemented in the sorting program. In this study, a γ-γ matrix was created without gain-drift correction as well, for comparison. It was found that gain-drift correction improved resolution by $\approx$5%.

As the target was sufficiently thick to stop recoiling nuclei, no Doppler correction was necessary.

4.4.2 Calibrations: energy and efficiency

Energy calibration was performed by recording γ-rays from the standard ^{152}Eu and ^{133}Ba calibration sources. The known energies [45] were compared to the measured channel number using the program *encal* [44]. A set of quadratic calibration coefficients are generated for each detector element. The coefficients were then used by MTSort to generate gain-matched spectra with a dispersion of 0.5 keV/channel.

Calibration of efficiency is also necessary, as the detectors record transitions with different efficiency, depending on the ability of the material to fully absorb γ-rays at different energies. All records of intensity must be divided through by this efficiency or it will falsely bias the intensity measurements.

The efficiency calibration was performed using the same sources as for energy calibration (since their intensities are also well known), and comparing the known intensities [45] with those measured. An "efficiency curve" was plotted via the program *effit* [44]. This fitted curve uses two quadratic functions, joined with a joining parameter, as described in [44]. The average Clover efficiency curve for this experiment is shown below (Fig. 10). Efficiency reaches a maximum at ≈120 keV and thereafter remains fairly constant with energy.

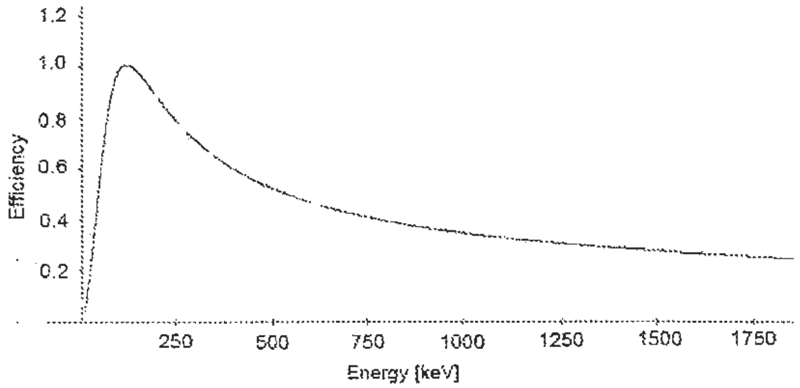

Figure 10: Average Clover efficiency *vs.* γ-ray energy for this experiment. Efficiency is normalized to a value of 1.0. Note maximum efficiency at ≈ 120 keV.

4.4.3 Random subtraction

Subtraction of random coincidences from the histograms is necessary: γ-rays emitted during successive beam-bursts may coincide by chance (not because they occur in cascade) if a state is very heavily populated or is more long-lived than the assumed longest lifetime. The procedure for random-subtraction used was that recommended by [46], and is outlined below.

Two histograms were made: one (matrix A) binning *all* coincidence events, and one (matrix B), binning *only* coincidence events in which the transitions occured in sucessive beam bursts. Only coincidences between transitions from the same beam burst ("prompt" transitions) may be true coincidence events. The first matrix (matrix A) will record such "prompt-prompt" coincidences; matrix B has both prompt and late transitions along one axis, and late transitions alone along the other, giving [46]:

$$\begin{aligned} \text{matrix A} : (p+l) \times (p+l) &= p^2 + 2pl + l^2 \\ \text{matrix B} : l(p+l) &= pl + l^2 \end{aligned}$$

The subtraction of twice matrix B from matrix A would then subtract out, in their entirety, all prompt-late ($p-l$) coincidences. The additional l^2 term which arises is negligible: coincidences between two events from the beam burst subsequent to that of interest form a very small percentage of the data [46].

Before the time-gated matrices A and B could be sorted, it was necessary to gain-match the time-spectra from every detector. It was found that prompt events fell within the channel-limits 1000-1120 in the time spectrum (see Fig 11). In Fig 11, prompt events occur in those channel-numbers corresponding to the central peak of the spectrum.

The above procedure was followed for the γ-γ symmetric matrix and asymmetric DCO matrix, and also attempted for the Polarisation matrix. However, as there were fewer counts in the Polarisation matrix, over-subtraction

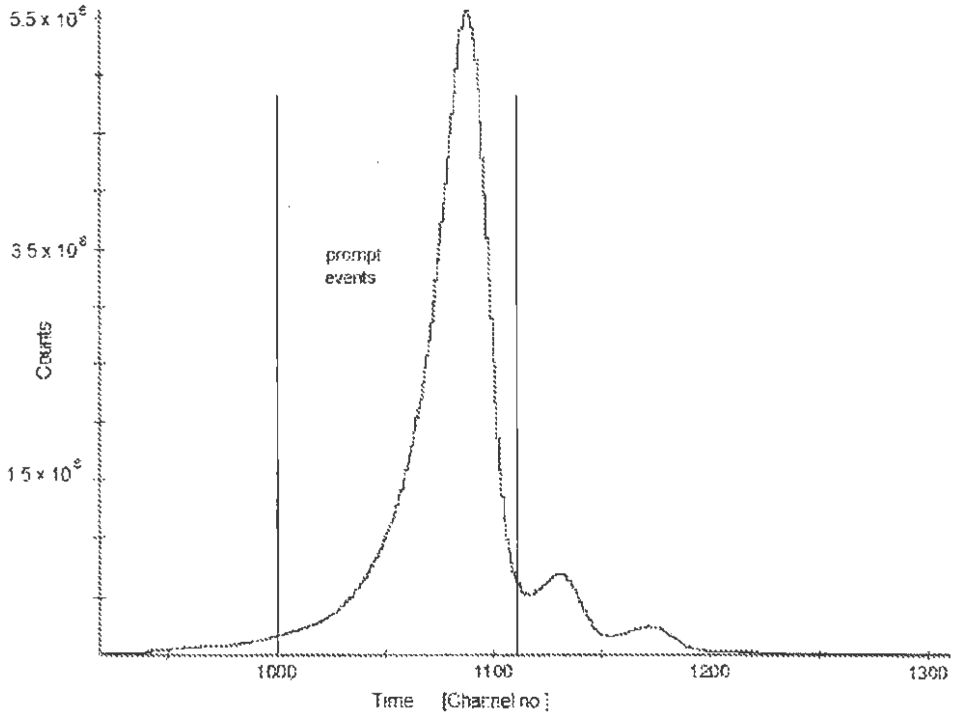

Figure 11: The total energy-time spectrum for this experiment. The vertical lines outline the peak of prompt events (channels 1000-1120). The late events are those transitions which arrived in the time-interval of channels 1164-1214.

resulted, and so the time-gated Polarisation matrix was not used. After subtraction, $\approx 2\%$ random coincidences remained in the γ-γ matrix.

4.5 Classifying transitions

Determining transition multipolarity λ and polarisation (electric or magnetic character) is essential for evaluating the spin and parity of the decaying states. The detector-array used (Fig. 7) is ideally suited to the integrated Polarisation and Directional Correlation from Oriented states (integrated-PDCO) method [47]. The procedure is discussed below (Section 4.5.1-4.5.2).

4.5.1 Angular distribution and multipolarity

In heavy-ion reactions, the intensity of a transition is by no means isotropically-distributed around the ensemble of nuclei. Depending on its multipolarity, stretched or unstretched character and mixing ratio and on the orientation of the emitting nuclei, certain directions will be favoured for emission of a particular transition, building up a definite angular distribution of intensity. Measuring this angular distribution is thus one way to determine the multipolarity λ of the γ-ray.

The orientation of the decaying states, as described by the statistical tensor ρ_{kq}, will greatly influence angular distribution as well [48]. Dependence of angular distribution on ρ_{kq}, λ and other properties is given by the theoretical angular distribution $W(\theta, \phi)$ (Eqn 32, Appendix 3).

It is not always possible to measure angular distribution $W(\theta, \phi)$ directly, as this requires the detectors to be arranged in several different rings around the target, as in many of the larger arrays like Gammasphere. In these cases, it is possible to directly determine the a_2, a_4 coefficients of the angular distribution, and from these the λ of the γ-ray can be determined.

Angular distribution may also be deduced indirectly, via correlation between two γ-rays, as follows: Assume (γ_1, γ_2) is a pair of coincident γ-rays measured in two detectors placed at different angles θ. In principle, if γ_2 is of minimum intensity at a certain angle, and the transition on which one gates (γ_1) has maximum intensity there, then the intensity of their coincidence is small. A large coincidence-intensity is only observed where *both* transitions reach a maximum. Thus, angular distribution information for γ_2 is encoded in its correlation with that of γ_1.

When the angular distribution $W(\theta, \phi)$ is deduced in this way and the original state was oriented, (the orientation is dictated by the reaction-mechanism), one is determining the Directional Correlation from Oriented states (DCO), or $W(\theta_1, \theta_2, \phi_1, \phi_2)$ [48]:

$$\begin{aligned} W(\theta_1, \theta_2, \phi_1, \phi_2) &= \sum_{kqk_1q_1k_2q_2} \rho_{k_1q_1}(I_1)(-1^{k_1+q_1})\sqrt{(2k+1)(2k_1+1)} \begin{pmatrix} k_1 & k & k_2 \\ -q_1 & q & q_2 \end{pmatrix} \\ &\quad \times A_k^{k_2k_1}(\delta_{\gamma_{12}}\lambda\lambda' I_2 I_1) Q_k(E_{\gamma_{12}}) D_{q0}^{k*}(\phi_1, \theta_1, 0) \\ &\quad \times A_{k_2}(\delta_{\gamma_{23}}\lambda\lambda' I_3 I_2) Q_{k_2}(E_{\gamma_{23}}) D_{q20}^{k_2*}(\phi_2, \theta_2, 0) \end{aligned} \tag{26}$$

Here, the variables are as defined in Appendix 3, and the angles θ_1, θ_2, ϕ_1 and ϕ_2 are as defined in Fig. 12.

This is used practically via the DCO-ratio [47]. A ratio of two DCOs (one with the gate at θ_2 and the transition of interest at θ_1, say, and the other with the angles exchanged) may "pinpoint" the multipolarity of an unclassified transition: the ratio will be 1:1 if the distributions are identical. Values of the ratio will vary with the alignment (as expressed by the alignment parameter σ/I) of these oriented states, with the character of the transition, initial

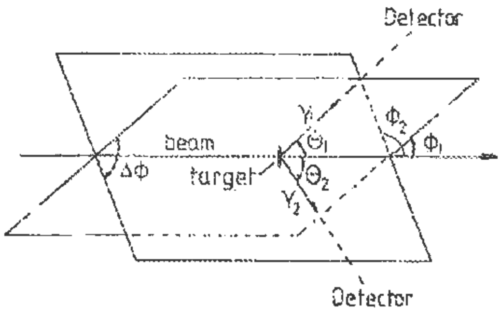

Figure 12: Geometry of the beam-line-detector setup, defining angles θ_1, θ_2, ϕ_1, ϕ_2 and $\Delta\phi$ [27].

and final angular momenta, and even with angles θ_1, θ_2 and $\Delta\phi = |\phi_2 - \phi_1|$ (the greatest variations of DCO with λ occur when there is a difference of 90^o between θ_1 and θ_2 [49]). Thus, no clean-cut characteristic values for the DCO-ratio (R_{DCO}) may be supplied. In order to assign multipolarity to the γ-rays in a cascade, calculations of theoretical DCO-ratio for several possible cascades must be performed and compared to the measured DCO-ratios.

Theoretically, the DCO ratio is given by the ratio of the two DCOs (as in Eqn 25), or [49]:

$$R_{DCO} = \frac{W(\theta_1, \theta_2, \Delta\phi)}{W(\theta_2, \theta_1, \Delta\phi)}. \tag{27}$$

The experimental DCO-ratio is determined by measuring the coincidence intensity when the gating transition is measured at one angle and the transition of interest is at the second angle; then the measurement is repeated with the angle swapped, and the ratio of the two intensities is determined. The equation is [49]:

$$R_{DCO} = \frac{\epsilon^{\theta_1}_{\gamma_2}\epsilon^{\theta_2}_{\gamma_1}\left(I^{\theta_1}_{\gamma_2}\mathrm{gated}^{\theta_2}_{\gamma_1}\right)}{\epsilon^{\theta_2}_{\gamma_2}\epsilon^{\theta_1}_{\gamma_1}\left(I^{\theta_2}_{\gamma_2}\mathrm{gated}^{\theta_1}_{\gamma_1}\right)}, \tag{28}$$

where $I_{\gamma_2}^{\theta_1}$ refers to the intensity of γ_2 (the transition of interest) at θ_1, and $\text{gated}_{\gamma_1}^{\theta_2}$ indicates that the gating transition was at the second detector-angle (θ_2), *etc.* The value $\epsilon_{\gamma_2}^{\theta_1}$ is the efficiency with which a transition of energy γ_2 will be observed at the angle θ_1, and $\epsilon_{\gamma_1}^{\theta_2}$ is the efficiency for the gating transition (γ_1) at angle θ_2, *etc.*

Under normal circumstances, all four efficiency (ϵ) values are equal, allowing them to cancel out of the calculation [46]. The intensities I above (Eqn 27) are measured as counts recorded in the DCO histograms for the experiment[4]. In this experiment, the DCO ratios were both calculated and measured with $\theta_1 = 135°$ and $\theta_2 = 90°$. The value of $\Delta\phi$ for this array is $\Delta\phi = 45°$.

The calculations of DCO ratio were performed using the program *DCOPlot* [48], with an alignment-parameter of $\sigma/I = 0.35$, (as recommended in [48] for fusion-evaporation reactions). An example of the plots produced is provided in Section 5.5 (Fig 18), along with the measured values used to deduce the spins of the levels in a cascade. The R_{DCO} measurements were taken from the asymmetric DCO-matrix constructed.

4.5.2 Polarisation and electric/magnetic character

The DCO-ratio may aid in the determination of γ-ray multipolarity, and polarisation measurements are indicative of electric/magnetic character (polarisation), but neither is conclusive if used alone. Used together, they consitute a powerful technique–P-DCO–for classification of transitions [36]. It is itself not always conclusive, however [36].

---

[4] The only cases where intensities are different are: if detectors with different properties of γ-ray absorption are used at different angles (*e.g.* Clovers at one angle, LEPS at the other), or if shielding around the target will seriously attenuate γ-rays emerging at certain angles.

Transition polarisation is referred to as magnetic if the electric field vector E lies vertically: that is, perpendicular to their direction of propagation (pointing up from the beam-line). Electric transitions are polarised such that E lies perpendicularly across the beam-line [27].

Measurements of polarisation rely on the fact that photons Compton scatter most strongly in the direction perpendicular to the alignment of **E** [27]. Thus, if a photon scatters inelastically into the detector-element to the right or left of the one with which it first collided, (horizontal scattering), then **E** must lie vertically across the direction of its propagation, as scattering occured most strongly in the direction perpendicular to this. Horizontal scattering thus indicates magnetic character. Similarly, if the photon scatters inelastically into the element above or below the one it first struck (vertical scattering), then **E** must lie laterally across the propagation-direction (beam-direction). Vertical scattering thus indicates that the photon has electric character.

The polarisation asymmetry (polarisation anistropy) A_P for a transition may be measured as

$$A_P = \frac{N_V - N_H}{N_V + N_H}, \tag{29}$$

where N_V and N_H are the measured intensities for scattering in the vertical and horizontal directions, respectively. This ratio will reflect the degree to which a transition vertically or horizontally scatters. Its value will necessarily be less than the predicted polarisation P [36]:[5]

$$P = \frac{W_\perp - W_\parallel}{W_\perp + W_\parallel}, \tag{30}$$

due to losses in the detector. Here $W_\perp$ and $W_\parallel$ indicate probabilities of photon emission with the electric field oscillating perpendicular and parallel to

---

[5] The reference [36] measures "parallel" and "perpendicular" relative to the emission plane, not beam-direction, and hence the designations here (Eqn 30) are opposite to theirs.

the beam direction.

The measured value A_P is related to polarisation P (Eqn 30) via a polarisation sensitivity factor Q, which takes into account the loss of recorded intensity due to detector efficiency considerations. Thus, to determine a measured polarisation $P_{meas.}$ for comparison to the predicted polarisation P, one may use the equation [36]:

$$P_{meas.} = \frac{A_P}{Q}. \tag{31}$$

The polarisation sensitivity $Q = Q(E)$ varies with transition energy, and a "polarisation sensitivity curve" ($Q(E)$ *vs.* E) may be determined for the detector in question. In this study, the polarisation sensitivity curve given by [36] for a Clover detector was used (see Appendix 3 for details and calculations of uncertainty).

A positive value of P indicates an electric transition; a negative, a magnetic transition, in the case of stretched transitions. In the case of unstretched transitions, the opposite is true [36]. The expected polarisation anisotropy may be calculated for a given I_1-I_2 and σ/I value, using the code *polar* [50]. These values may then be compared with experiment and used to confirm both transition character and spin assignments, since stretched or unstretched nature is also suggested by the sign of A_P.

The intensities (N_V and N_H) for the ratio (Eqn 29) are determined from coincidence spectra: one in which the coincident transitions scattered vertically (N_V), and one in which they scattered horizontally (N_H). These require two asymmetric matrices (one recording coincidences between γ-rays in *any* detector and γ-rays which scattered vertically in $\theta = 90°$ detectors, and another for the horizontally-scattered transitions). The scattering-direction is itself recorded via the Clover bit pattern, as discussed in Appendix 3.

In this experiment, two polarisation matrices were produced (all-vertical and all-horizontal), and polarisation anisotropies measured for all unclassified placements. All detectors in the array for this experiment were oriented as shown in Fig. 8. This orientation would assign the bit patterns supplied in Appendix 3 to horizontal and vertical scatters. The values of A_P for all transitions classified are supplied in the relevant tables of Results (Section 5.6, Tables 5 and 6).

The properties of the gate do not affect polarisation measurements, so summed gates were used for measuring A_P whenever intensity for a particular coincidence was small. A vertical and a horizontal matrix were made, and time-gating was attempted, but the counts in each matrix were low enough that subtraction of randoms led to over-subtraction, and so was not used.

5 Results

The previously-known [10] level scheme (Fig. 1) was extended and modified: the placement of eleven of the transitions was changed, and twenty-seven transitions were placed that were previously unrecorded. The resulting new level scheme is provided below (Fig. 13).

As there were so many changes made to the level scheme, classifying levels and transitions became of major importance, and so a PDCO analysis was undertaken for the newly-placed transitions. As a first step for this analysis, DCO-ratios, polarisation anisotropies and intensities were measured for selected established $E1$ and $E2$ transitions (according to [10,23]), and are supplied in Tables 5 and 6 (pages 78 and 79). The gates for these measurements were known to be stretched $E2$s throughout. Knowing the DCO-ratios for transitions of known character (when gating on $E2$s) for a particular experiment, is a good first indicator of character. The average DCO-ratio for known stretched $E1$s was found to be 0.57(7), and the average polarisation anisotropy was found to be 0.15(11). For stretched $E2$s the average DCO-ratio was 1.03(6), and the average polarisation anisotropy was 0.33(9).

Due to the revisions made, 16 new levels were added. The new placements and spin and parity (I^{π}) assignments for the new levels will be discussed for each band (Sections 5.1-5.6).

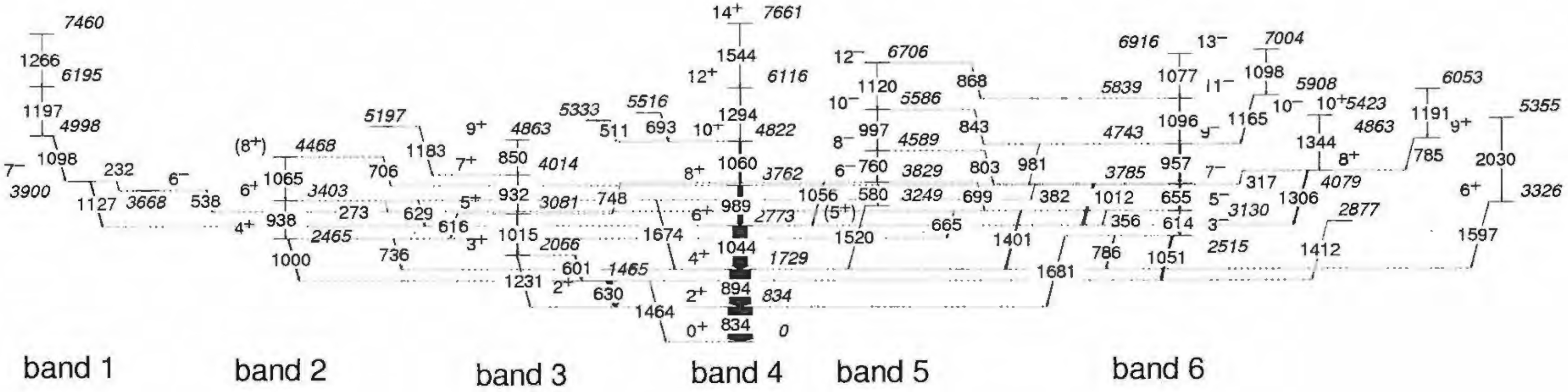

Figure 13: The extended level scheme for ^{72}Ge. Width of arrows is proportional to intensity. Uncertain I^{π} assignments are in parentheses. Transition energies and level energies are in keV.

5.1 Band 1

This band decays into the well-known 3.668 MeV 7^- level [10], depopulated by an 1127 keV transition. The spectrum in coincidence with the 1127 keV transition (Fig. 14a) shows transitions of 1098 keV, 1197 keV and 1266 keV. The intensites of these coincidences suggest the arrangement of the transitions as in Fig. 13.

The 1098 keV, 1197 keV and 1266 keV transitions are all in coincidence with a 232 keV transition, which is in anti-coincidence with the 1127 keV transition (see Fig. 14b). It was thus placed parallel to the 1127 keV transition.

The spectrum gated on 1127 keV also shows strong coincidence with a 974 keV transition. A gate on the 974 keV transition (Fig. 14c) shows that the 1127 keV peak dominates the spectrum, while coincidences with transitions in the ground state band (notably the 834 keV transition to the ground state), are minimal. This comparative absence of concidences with transitions to the ^{72}Ge ground state suggests that the 974 keV transition is separate from the decay-system of ^{72}Ge. It may be, then, that the coincidence between the 1127 keV and 974 keV transitions occurs in a contaminant nucleus. The 974 keV transition was therefore left out of the level scheme.

The 1127 keV and 974 keV transitions are in coincidence in ^{71}Ge, which is also produced in this experiment. However, the high intensity of the 974 keV peak in the 1127 keV spectrum suggests that this coincidence cannot arise purely from there, since transitions from ^{71}Ge only comprise about 0.1% of the data.

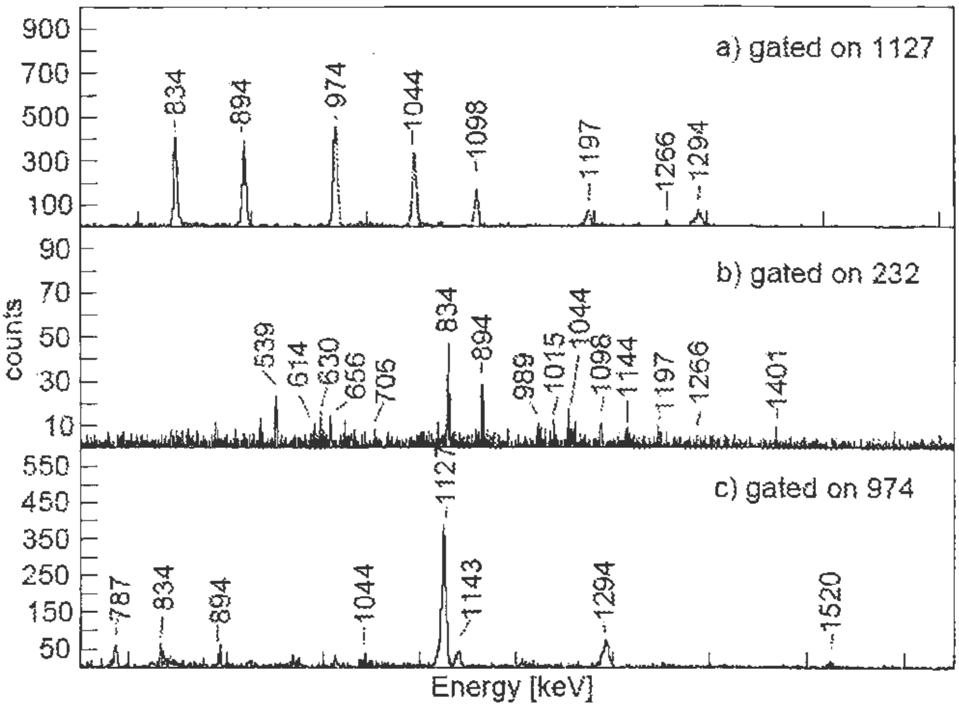

Figure 14: Spectra gated on (a) the 1127 keV, (b) the 232 keV and (c) the 974 keV transitions. Note the coincidences with the 1098 keV, 1197 keV and 1266 keV transitions in (a) and in (b) note the coincidences with 1098 keV, 1197 keV and 1266 keV transitions and absence of coincidence with the 974 keV transition.

5.2 Band 2

This band was known up to the 3.403 MeV 6^+ level [10]. Two transitions linking this band to the ground-state band were placed due to observed coincidences (Fig. 15a and b): a 736 keV transition between the 4^+ level of this band and the 4^+ level of the ground state band and a 629 keV transition between the 6^+ level of this band and the 6^+ level of the ground state band.

In the original level scheme there was an additional 8^+ level at 4.523 MeV, arising because the 1120 keV transition was placed above the 938 keV transition. This was removed due to no coincidences between the 1120 keV and 938 keV transition being observed (see Fig. 16b).

A new level at 4.468 MeV is depopulated by the 1065 keV γ-ray. It was placed above the 938 keV transition due to coincidences observed between the 1065 keV transition and the known band members (see Fig. 15c). This new level also decays to the ground state band, via a newly-placed 706 keV transition. Due to there being no appropriate gate in which to measure the DCO-ratio for the 1065 keV transition, a tentative spin and parity assignment of (8^+) was made to the 4.468 MeV level. This assignment is consistent with unstretched $E2/M1$ character for the 706 keV transition, which agrees with its measured DCO-ratio of 1.03(10) (when $\delta \approx 0.81$). In addition, a spin any greater than 8 for the 4.468 MeV level would be unlikely, since it would require the 1065 keV transition to have multipolarity $\lambda = 3$ or higher.

5.3 Band 3

This band was know up to the 3.081 MeV level [10]. There is an intense coincidence between a 932 keV transition and the 1015 keV transition that depopulates the 3.081 MeV level (see Fig. 16a). The 932 keV transition was

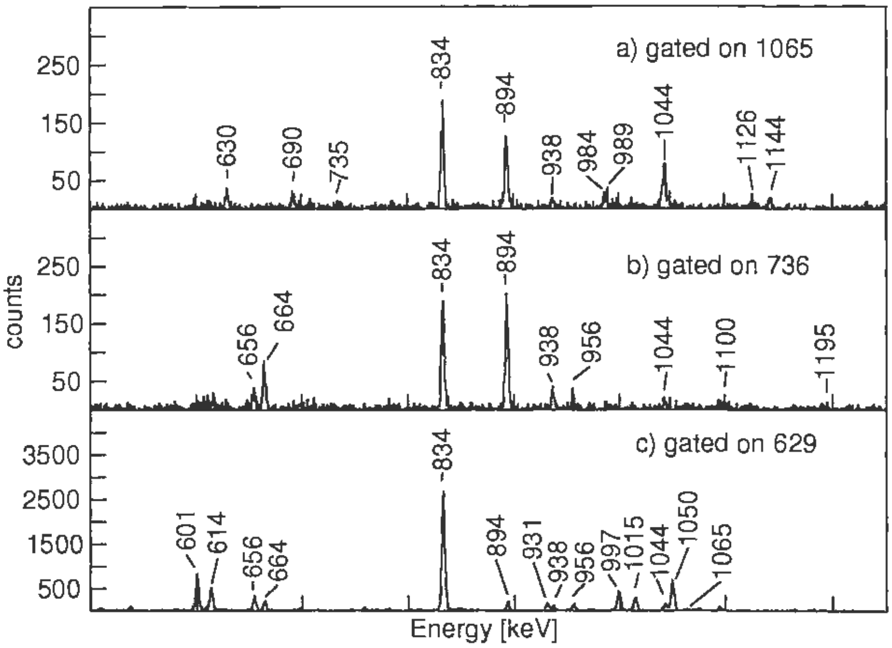

Figure 15: Spectra gated on (a) the 1065 keV, (b) the 736 keV and (c) the 629 keV transitions. Note in (a) the coincidence of the 1065 keV transition with the 938 keV transition. In (b), there is a coincidence with the 938 keV transition but an anticoincidence with the 1000 keV transition, in agreement with the placement of the 736 keV transition. In (c), note the coincidences with the 1065 keV transition, but also with the transitions of band 3, which occur due to contamination of the gate with the 630 keV transition.

thus added above the 3.081 MeV level, giving rise to a new level at 4.014 MeV. The original study of [10] placed a 3.841 MeV level here, linked to the rest of the band by a 760 keV transition. Were this the case, this 760 keV transition would be in coincidence with the 1015 keV and 1464 keV transitions. No such coincidences were observed (see Fig. 17c), and so this level was removed.

In the original study, a 932 keV transition was placed entering the 1.465 MeV 2^+ level from a 2^+ level at 2.397 MeV [10]. This placement would require coincidences between the 932 keV transition and the 630 keV, 834 keV and 1464 keV transitions only. This is not the case, (see Fig. 16a), so the 2.397 MeV level was removed from the scheme.

The 932 keV transition is also in coincidence with a 616 keV transition (see Fig. 16a), which is in anti-coincidence with the 1015 keV transition. It was thus placed below the 932 keV transition, depopulating the 3.081 MeV level and entering the 2.465 MeV level of band 2. Coincidences between the 932 kev transition and transitions at 850 keV and 1183 keV were also observed (see Fig. 16a). The 850 keV and 1183 keV transitions are in anti-coincidence with each other, but are both are seen by the other members of band 3. These transitions were thus placed above the new 4.014 MeV level, giving rise to a 4.863 MeV level and a 5.197 MeV level respectively.

A 1231 keV transition is coincident with the 1015 keV transition and the 834 keV transition of the ground state band, and so this was placed linking the 2.066 MeV level of band 3 and the 0.834 MeV 2^+ level of the ground state band.

The 1015 keV transition is in coincidence with a 748 keV transition, which is absent when gating on the 932 keV transition, and present when gating on the 760 keV and 997 keV transitions of band 5 (see Fig. 17c and d). It is also evident in the 1015 keV gate (band 3, spectrum not shown). This transition was thus placed linking the 3.829 MeV level of band 5 to the 3.081 MeV level of band 3.

The placement of this 748 keV transition questions the previous assignment of $I^\pi = 4^+$ to the 3.081 MeV level of band 3. The 3.829 MeV level in band 5 has $I^\pi = 6^-$, (see Section 5.5): in that case, the 748 keV transition would occur between a 6^- level and a 4^+ level, assigning it stretched $M2$ character. This transition has a (normalised) intensity of 7, but the other transitions leaving the 3.829 MeV level (699 keV and 1056 keV) have intensities of 15 and 32 respectively (see Table 6). Since both these transitions have $M1/E2$ character, the suggested $M2$ character of the 748 keV transition seems unlikely because these $M1/E2$s should have intensities many orders of magnitude greater than an $M2$, not merely double it, since $M2$s are strongly supressed [26].

The character of the 1015 keV transition which leaves the 3.081 MeV level is not well-established. Thus, the I^π of the 3.081 MeV level is open to change. An assignment of spin and parity of $I^\pi = 5^+$ to the 3.081 MeV level is proposed. This assignment conveys stretched $E1$ character to the 748 keV transition, which is compatible with its measured DCO-ratio (0.80(22)) and positive polarisation anisotropy (0.20(32)). The DCO-ratio of the 1015 keV transition could not be established, as every possible gate picks up intensity from the neighbouring 1012 keV transition. However, its strongly-positive polarisation anisotropy (0.30(12)) is compatible with stretched $E2$ character. Thus, the spin and parity assignments of the 3.081 keV level were re-assigned as $I^\pi = 5^+$.

This assignment gives the 616 keV transition stretched $M1$ character, which is consistent with both its measured DCO-ratio (0.90(16)) and its negative polarisation anisotropy (-0.81(75)).

To establish the spin and parity of the 4.014 MeV level, DCO-ratio and polarisation anisotropy were measured for the 932 keV transition, which connects this level to the 3.081 MeV level. These measurements ($R_{DCO} = 0.85(7)$ and $A_P = 0.39(10)$) are compatible with stretched $E2$ character. As this transition links the 4.014 MeV level to one assigned an I^π of 5^+, the 4.014 MeV level was assigned an I^π of 7^+.

Having established the spin and parity of the 4.014 MeV level, it is possible to proceed to the new 4.863 MeV level, which decays to this level via the 850 keV transition, and to the 5.197 MeV level, which decays to the 4.014 MeV level via the 1183 keV transition. The measurements for the 850 keV transition ($R_{DCO} = 0.90(16)$ and $A_P = 0.36(47)$) are consistent with stretched $E2$ character. Thus the 4.863 MeV level was assigned an I^π of 9^+. The PDCO measurements for the 1183 keV transition could not be established with any degree of accuracy, due to weak intensity. The 5.197 MeV level was thus left unclassified.

The assignment of $I^\pi = 5^+$ to the 3.081 MeV level, and the subsequent assignment of odd-spin and even parity to all the levels above it in band 3, suggests that the 1.465 MeV level (which has a well-known spin and parity of 2^+) is not a member of band 3. It was thus moved, and not considered strictly a member of band 3.

5.4 Band 4

This band is the ground state band of ^{72}Ge. It was known up to the 12^+ level at 6.116 MeV [10]. Coincidences observed between the 1294 keV transi-

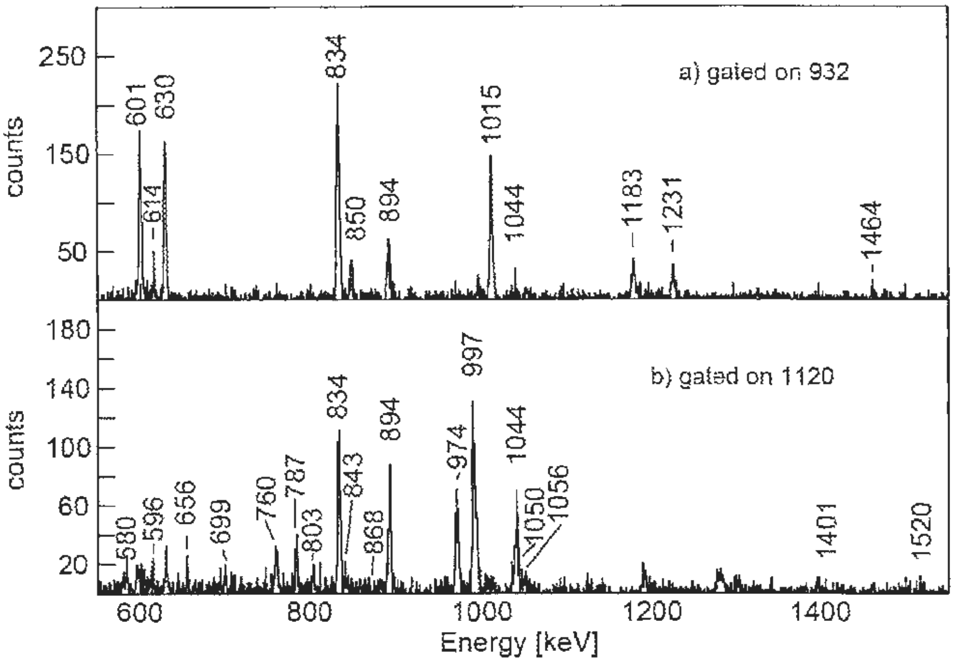

Figure 16: Spectra gated on the 932 keV transition (a) and the 1120 keV transition (b), showing coincidences inconsistent with their placement in Fig. 1. Note the strong coincidences of the 932 keV transition with the transitions in band 3 (Fig. 13), and those of the 1120 keV transition with the transitions in band 5.

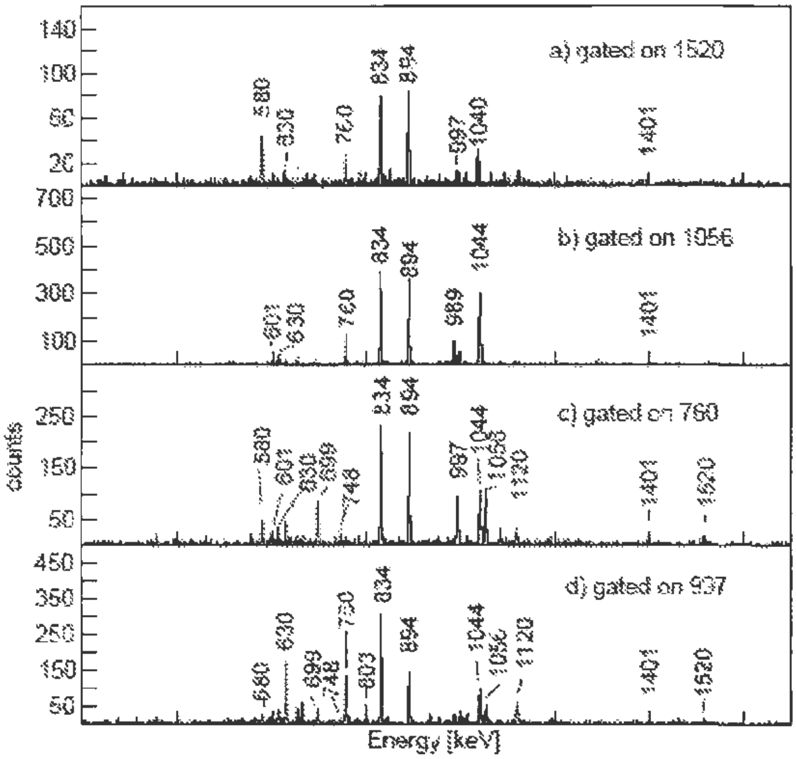

Figure 17: Spectra gated on (a) the 1520 keV, (b) the 1056 keV, (c) the 760 keV and (d) the 997 keV transitions. Note the large peaks indicating coincidences with the 580 keV and 997 keV transitions in (a) and (c); and the absence of a 580 keV peak in (b), showing anti-coincidence with the 580 keV transition. Note the strong coincidence with the 803 keV linking transition in (d).

tion depopulating this level and a 1544 keV transition suggest placement of the 1544 keV transition entering this level. This placement above the 6.116 MeV level is confirmed by coincidences with all the other transitions in the ground state band, and gives rise to a new level at 7.661 MeV. A DCO ratio of 0.99(14) and polarisation anisotropy of 0.52(17) suggest stretched $E2$ character for the 1544 keV transition. The new 7.661 MeV level was thus assigned a spin and parity of $I^\pi = 14^+$.

5.5 Band 5

This structure was not known in the original studies. It consists of 5 levels, and decays to the ground state band, to band 3 and to band 6.

The 1520 keV transition that links the 3.249 MeV level of this band to the ground state band was originally placed above the 2.773 MeV level of the ground state band [10]. It was moved from this placement due to negligible coincidences with the 1044 keV transition that depopulates the 2.773 MeV level (see Fig. 17a). The strong coincidences observed in this gate with the 580 keV, 760 keV and 997 keV transitions all suggest placement at the bottom of band 5.

The spectrum gated on the 1056 keV transition (Fig. 17b) shows strong coincidence with the 760 keV transition, but no coincidences with the 580 keV or 1520 keV transitions. These anti-coincidences, combined with the coincidence of the 1056 keV and 1044 keV transitions, all suggest the placement shown in Fig. 13.

The 1120 keV transition is another example of a misplaced transition: The original placement [10] would require coincidences with the 938 keV, 1000 keV and 834 keV transitions. However, coincidences with the 997 keV, 760 keV and 580 keV transitions are observed in the spectra from our experiment (Fig. 16b). As band 5 was being added to the level scheme, it became clear that the 1120 keV transition must be part of that structure due to these coincidences, and inspection of intensities suggested placement at the top of this band.

The 3.829 MeV, 4.589 MeV, 5.586 MeV and 6.706 MeV levels of band 5 decay to levels of band 6. The linking transitions all showed the required coincidence relationships: note especially the strong coincidence between the 997 keV transition and the 699 keV and 803 keV linking transitions (Fig. 17d).

The DCO-ratios and positive polarisation anisotropies measured for the 760 keV and 997 keV transitions ($R_{DCO} = 0.99(9)$ and $0.89(7)$ and $A_P = +0.17(20)$ and $+0.17(25)$ respectively), are consistent with those for stretched $E2$s (see Table 5). These were thus both assigned stretched $E2$ character.

To proceed with the I^π assignments for band 5, it was noted that three of its levels (at 3.829 keV, 4.589 keV and 5.586 keV) decay via fairly intense transitions to levels in band 6, for which the spins and parities are known [10]. Thus, assignment of spins and parities to these three levels could begin from this premise.

The 3.829 MeV level of band 5 decays to the 3.130 MeV level of band 6 via a 699 keV transition. The spin and parity for the 3.130 MeV level are known to be $I^\pi = 5^-$. A measured DCO-ratio of 0.37(5) for the 699 keV transition is consistent with mixed character with $\delta \approx -0.84$, as comparison with the calculated DCO-ratio shows (Fig. 18c). As the quadrupole admixture is substantial, an $M1/E2$ character is more likely than $E1/M2$. With $M1/E2$ character, the spin and parity changes associated with the 699 keV transition would mean it links the $I^\pi = 5^-$ level to one of $I^\pi = 6^-$. Thus, the 3.829

MeV level of band 5 was assigned an I^π of 6^-.

A DCO-ratio and polarisation anisotropy were also measured for the 803 keV transition linking the 4.589 MeV level of band 5 to the 3.785 MeV level of band 6 (which has $I^\pi = 7^-$). The DCO-ratio of 0.46(9) is consistent with mixed $M1/E2$ character with $\delta \approx -0.84$ (see Fig 18b). Once again, the substantial quadrupole admixture suggests $M1/E2$ character rather than $E1/M2$. The associated spin and parity changes for an $M1/E2$ assign a spin and parity of $I^\pi = 8^-$ to the 4.589 MeV level.

This assignment of $I^\pi = 8^-$ to the 4.589 MeV level allows for characterisation of the 5.586 MeV level above it. This level decays to the 4.589 level via the 997 keV transition. The assignment of stretched $E2$ character to the 997 keV transition suggests spin and parity of $I^\pi = 10^-$ for the 5.586 MeV level, as the transition would connect levels of $\Delta I = 2$ and the same parity. The 5.586 MeV level was thus assigned an I^π of 10^-. The 5.586 MeV level also decays to the 4.743 MeV level of band 6 ($I^\pi = 9^-$) via an 843 keV transition. A measured DCO-ratio of 0.83(17) for the 843 keV transition is consisent with calculations assigning it stretched $M1/E2$ character with $\delta \approx 0.36$ (see Fig. 18a), which agrees with an assignment of $I^\pi = 10^-$ to the 5.586 MeV level. A measured polarisation anisotropy of -0.42(28) does not contradict stretched $M1/E2$ character for the 843 keV transition. Thus, the assignment of $I^\pi = 10^-$ was retained.

Assignment of I^π to the 6.706 MeV level could then proceed. The known I^π values of band 6 were of no use here, as the 868 keV transition between this 6.706 keV level and the 11^- level of band 6 (at 5.839 MeV) was too weak for measurements of DCO-ratio or polarisation anisotropy to be made. The 1120 keV transition from this level to the 5.586 MeV level of band 5 may be assigned (within uncertainty) a stretched $E2$ character ($R_{DCO} = 0.93(9)$

and A_P = -11(42)). As the 5.586 MeV level has an I^π of 10^-, the 6.706 MeV level was assigned an $I^\pi = 12^-$.

Finally, the assignment of I^π to the 3.249 MeV level of band 5 was rather problematic. Two transitions link this level to levels of known I^π: the 1520 keV transition, which links it to the 4^+ level of the ground state band, and the 580 keV transition, which links it to the 3.829 MeV level of band 5 (to which $I^\pi = 6^-$ was assigned). The problem arises because the measured DCO-ratio of 0.83(14) for the 580 keV transition is consistent with three possible interpretations: (1) The 580 keV transition could be a streched $E2$, making the 3.249 MeV level a 4^- level; or, (2) this transition could be a stretched $E1$ (as in the solid curve of Fig 18f), which would make this level $I^\pi = 5^+$; or, (3) the 580 keV transition could be an unstretched $M1/E2$, making the 3.249 MeV level a 6^- level. Unfortunately, $A_P = 0.45(18)$ is consistent with all three scenarios. To decide between these three possibilities we need to consider the character of the 1520 keV transition, which depopulates this level.

The 1520 keV transition feeds the 1.729 MeV 4^+ level. This effectively rules out (3). since $6^- \to 4^+$ requires the 1520 keV transition to be an $M2$. Also, the DCO-ratio of 0.67(9) for the 1520 keV transition does not indicate a stretched quadrupole. This leaves scenarios (1) and (2). The measured DCO-ratio agrees better with (2), as in the solid curve in Fig: 18d, but one cannot completely rule out (1). The A_P of -0.35(25) for the 1520 keV transition is consistent with both (1) (where the 1520 keV transition would then be an $E1/M2$ with $\Delta I = 0$), and (2), if the 1520 keV transition is a stretched $E1/M2$ (with $\Delta I = 1$). We therefore choose the second possibility, which would correspond to assigning the 3.249 MeV level an I^π of 5^+.

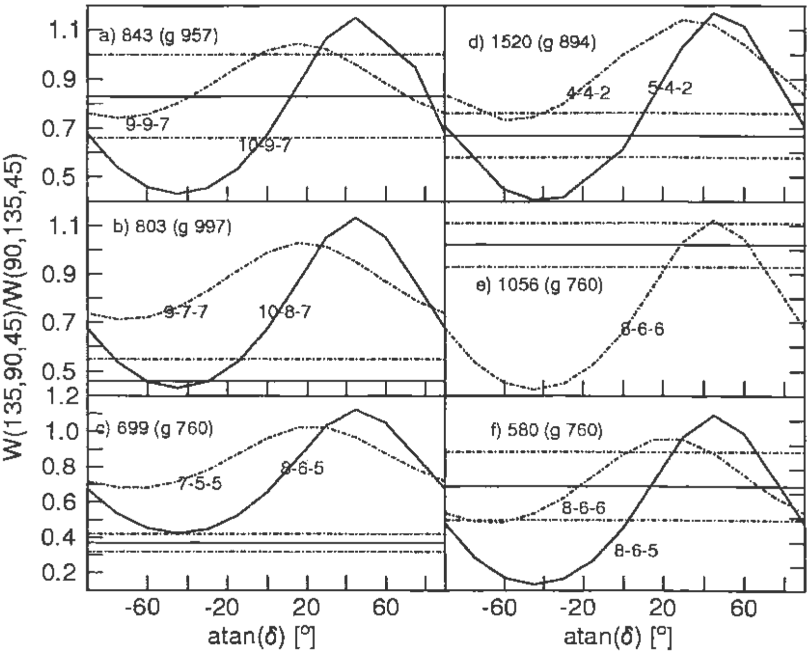

Figure 18: Plots of DCO-ratio calculated as a function of mixing ratio, for various possible cascade ($I_1 - I_3$) values for the transitions of band 5. The solid lines crossing the plots indicate the measured DCO-ratio; the dotted lines the uncertainty in the measured value. Crossing of the measured value with the calculated curve indicates the $I_1 - I_3$ values and mixing ratios. The gate used is supplied in parentheses.

5.6 Band 6

Band 6 was extended by one level from the original study [10]. Coincidence relationships observed for a 1077 keV γ-ray suggest its placement at the top of the band. This creates a new level at 6.916 MeV. The DCO-ratio of 1.05(12) and polarisation anisotropy of 0.26(20) for the 1077 keV transition are compatible with stretched $E2$ character. This assigns an I^{π} of 13^{-} to this new level. A 1012 keV transition was also placed, linking the 3.785 MeV 7^{-} level of this band to the 2.773 MeV 6^{+} level of the ground state band.

Table 5: The intensities[8], DCO-ratios (R_{DCO}) and polarisation anisotropies (A_P) measured for known $E2$ and $E1$ transitions, with their errors[9].

Transition [keV]	Intensity I_γ	Character	R_{DCO}	A_P
538		$E1$	0.53(7)	0.26(11)
1401		$E1$	0.61(6)	0.04(10)
Average			0.57(7)	0.15(11)
614	62	$E2$	1.04(6)	0.35(7)
834	1000	$E2$	0.93(1)	0.13(3)
894	770	$E2$	1.01(1)	0.30(3)
957	117	$E2$	1.02(7)	0.40(8)
989	193	$E2$	1.02(2)	0.37(5)
1000		$E2$	1.21(14)	0.21(8)
1044	589	$E2$	1.01(1)	0.41(6)
1060	90	$E2$	0.98(5)	0.40(8)
1096		$E2$	0.98(10)	0.31(10)
1294	32	$E2$	1.03(8)	0.52(17)
1306		$E2$	1.03(4)	0.43(11)
1464	19	$E2$	1.06(12)	0.10(16)
Average			1.03(6)	0.33(9)

Table 6: DCO-ratios (R_{DCO}) and polarisation anisotropies (A_P) measured for transitions in bands 4-6.

band	Level energy [MeV]	Transitions leaving level [keV]	Intensity I_γ	R_{DCO}	A_P
band 4	0.834	834	1000	0.93(1)	0.13(3)
	1.729	894	770	1.01(1)	0.30(3)
	2.773	1044	589	1.01(1)	0.41(6)
	3.762	989	193	1.02(2)	0.37(5)
	4.822	1060	90	0.98(5)	0.52(17)
	6.116	1294	32	1.00(8)	
	7.661	1544	6	0.99(14)	0.52(17)
band 5	3.249	1520	20	0.67(9)	-0.35(25)
	3.829	580	8	0.83(14)	0.45(18)
		699	15	0.37(5)	0.09(13)
		748	7	0.80(22)	0.20(32)
		1056	32	1.02(9)	-0.47(19)
	4.589	760	32	0.99(9)	0.17(20)
		803	12	0.46(9)	-0.28(22)
	5.586	843		0.83(17)	-0.42(28)
		997		0.89(7)	0.17(25)
	6.706	868			
		1120		0.93(9)	-0.11(42)
band 6	2.515	787	37	0.63(6)	-0.22(8)
		1050	83	0.60(2)	0.04(5)
		1680	11	0.65(9)	-0.26(29)

Continued on next page...

---

[5] In all cases the intensity is normalised to the 834 keV transition (which is assumed to have an intensity of 1000 counts).

[5] Uncertainties in the measurements were recorded directly from the RadWare output (see [44]).

Table 6 – Continued

band	Level energy [MeV]	Transitions leaving level [keV]	Intensity I_γ	R_{DCO}	A_P
	3.130	356	19	0.64(5)	0.12(7)
		614	62	1.04(6)	0.35(7)
		665	30	0.46(10)	0.00(11)
		1401	58	0.68(4)	0.04(10)
	3.785	381	5	0.85(24)	0.31(26)
		656	85	0.96(4)	0.39(7)
		1012	93	0.60(2)	0.13(7)
	4.743	957	117	1.02(7)	0.40(8)
		981	7	0.65(14)	0.11(62)
	5.839	1096		0.98(10)	0.31(10)
	6.916	1077	25	1.05(12)	0.26(20)

6 Discussion

In this section, the underlying physics associated with the band structures is discussed. The observed levels in ^{72}Ge could be organised into 6 band-like structures, but there were also several which could not be grouped in this way. The levels in a band usually correspond to a particular intrinsic structure, and should thus share some common features, such as moment of inertia. Various basic analyses were carried out to elucidate the underlying structures of the bands (primarily bands 4 and 5). These are discussed in Section 6.2. However, one aim of this study was to search for states that might correspond to a tetrahedral nuclear shape. This will be discussed first (Section 6.1).

6.1 Tetrahedral states

As has been mentioned, the existence of static tetrahedral states in this nucleus was not explicitly verified by this study, as no structures resembling the description of tetrahedral bands were discovered during the extension of the level scheme. A static tetrahedral structure would evidence itself as a low-lying, negative parity band. Since the tetrahedral shape would have a vanishingly-small quadrupole moment, the $\frac{B(E2:I\rightarrow I-2)}{B(E1:I\rightarrow I-1)}$ value should also be vanishingly-small for a tetrahedral band [21]. As pointed out by [21], such a branching ratio could be small for one of two reasons: very low $B(E2)$ values, or very high $B(E1)$ values.

While no structures of such description were observed here, their absence from the data could be because the tetrahedral states may also be particularly long-lived [2]. This is a problem when working in the ^{72}Ge nucleus, for which the states are mostly short-lived: most decay via highly-collective $E2$s, which give a large transition probability and a short lifetime. The (prompt-

prompt) coincidences considered when building this level scheme were all within 300 ns of each other, and so coincidences with particularly long-lived states are likely to have been missed.

A question also arises as to whether the tetrahedral states would be populated by the reaction used: the states are themselves considered to be low-lying, but that does not necessarily mean that the nucleus would be likely to enter these states as a result of energy introduced during collision with an α-particle.

It is also worth arguing at this point as to whether there is some other interpretation of the predictions of tetrahedral deformation at various N and Z. All the other possible candidate-nuclei for static tetrahedral deformation have turned out to exhibit strong octupole vibrations; the most recent example being ^{160}Yb [12]. Thus, on examining the results obtained here, and considering the results accrued in other studies, it may be worth considering the possibility that the nucleus vibrates between some extremes of tetrahedral deformation, rather than exhibiting static tetrahedral deformation.

In order for a reflection-asymmetric nuclear shape to be possible, there must be reflection-asymmetric components of the mean field. Such components have been considered to be the result of clustering [51]. Since there has not been any clustering behaviour reported in ^{72}Ge, the likelihood of a static reflection-asymmetric shape, (such as a tetrahedral shape, in the absence of a preferred symmetry axis) seems small for this nucleus.

Given this requirement of clustering, it is also worth noting that only certain pairings of the predicted "tetrahedral magic numbers" are conducive to clustering behaviour: 16 protons and 16 neutrons, for example, would give rise to (eight) α clusters and thus to a reflection-asymmetric mean field. Perhaps a further requirement for static tetrahedral shapes is, then, that the combination of tetrahedral magic numbers must be such that α-clusters could be formed: that is, one requires the same number of protons and neutrons, and that they both be tetrahedral magic numbers. This would also make static tetrahedral deformation only likely in the lighter nuclei, which can be well-described in terms of α-clusters [51].

On the topic of α-clusters, it also seems reasonable to suggest that only those nuclei with tetrahedral numbers (here meaning numbers of objects which could be arranged into a tetrahedron) of α-clusters would exhibit tetrahedral deformation: the α-particles could then be clustered into a tetrahedron much in the way a greengrocer arranges oranges. This would mean that, of the tetrahedral magic numbers, only $N = Z = 20$ would be likely to give a static tetrahedral state, as 10 α-clusters would arise. Recently, ^{40}Ca has been noted to be octupole-soft with respect to reflection-asymmetric octupole deformation [52] (that is, it has a potential with a minimum for reflection-asymmetric octupole deformation). This nucleus might thus be worth investigating for tetrahedral bands, as a test of the above idea.

6.2 Discussion of individual bands

There is rather little in the literature concerning interpretations of the known structures in the original ^{72}Ge level scheme: most efforts regarding ^{72}Ge have been concentrated on the excited 0^+ state[6] (at 0.69 MeV), and on the structure underlying the ground state band (band 4); both of which are fairly involved in their own right. All the six bands identified in this study are discussed below (Sections 6.2.1-4), along with their possible interpretations.

---

[6] The 0.690 MeV 0^+ state was not observed in this study, as neither the 690 keV transition nor those in coincidence with it were observed. For some reason, then, this isomeric state was not populated by the reaction in sufficient intensity to be measured.

6.2.1 Band 1

This band consists of 3 levels, none of which have been assigned spin and parity. Thus, there is little meaningful to be said regarding this structure. Since it has a band-head energy much higher than the 1.2 MeV threshold for pair-breaking, it may be suggested that it is based on a multi-quasiparticle structure.

6.2.2 Bands 2 and 3

These two bands appear to have a common underlying structure: they are similar in excitation energy (see Fig. 19), and their alignments are within a similar range (see Fig. 20).

It may therefore be suggested that bands 2 and 3 may constitute a γ-vibrational band: Both are positive-parity bands, one with even spin (band 2) and the other with odd spin (band 3). The levels are separated by a ΔI of 1 and are linked across the bands by inter-band $M1$ transitions (the 736 keV, 629 keV and 706 keV transitions (see Fig. 13)). These are all characterisics of γ-bands.

There is a very similar structure, also identified as a γ-vibrational band, in ^{74}Se [53], so the occurence of one in ^{72}Ge seems likely, since it is essentially the same nucleus with an additional pair of protons and so likely to have similar physics.

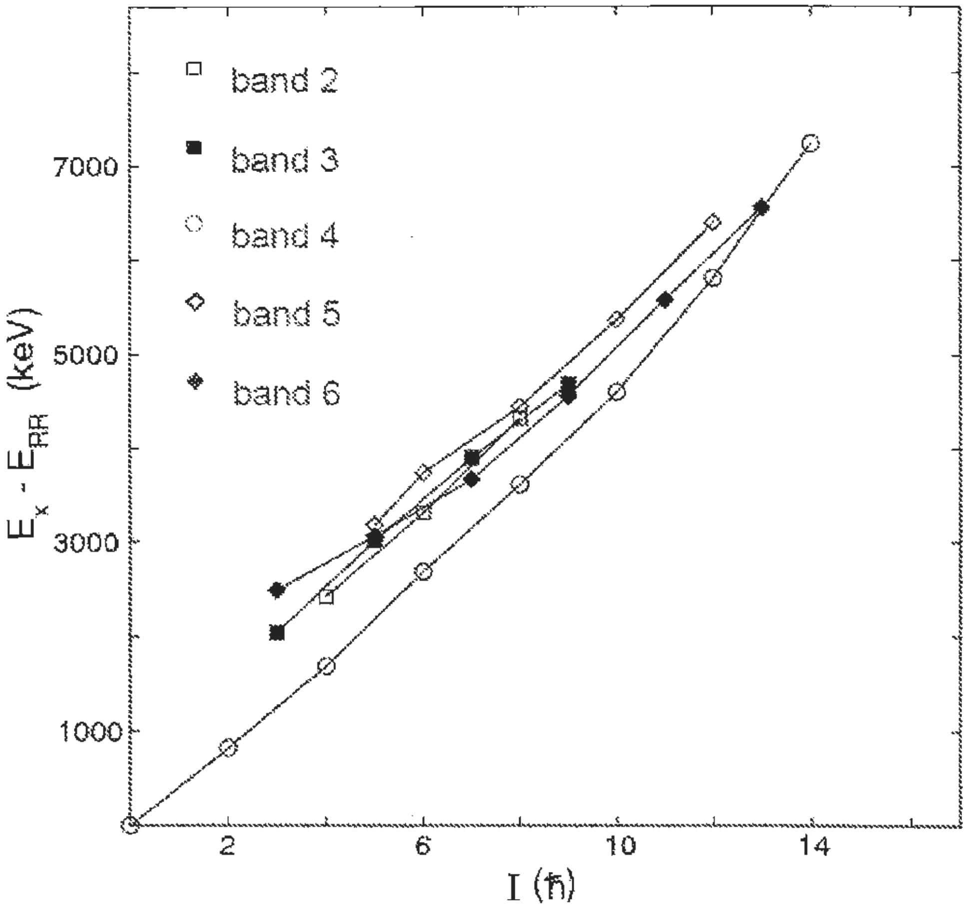

Figure 19: Excitation energies ($E_x - E_{rr}$) *vs.* spin (I) for bands 2-6. The parameter for calculating rigid rotor energies E_{rr} was $A = 2$ (see Eqn. 13).

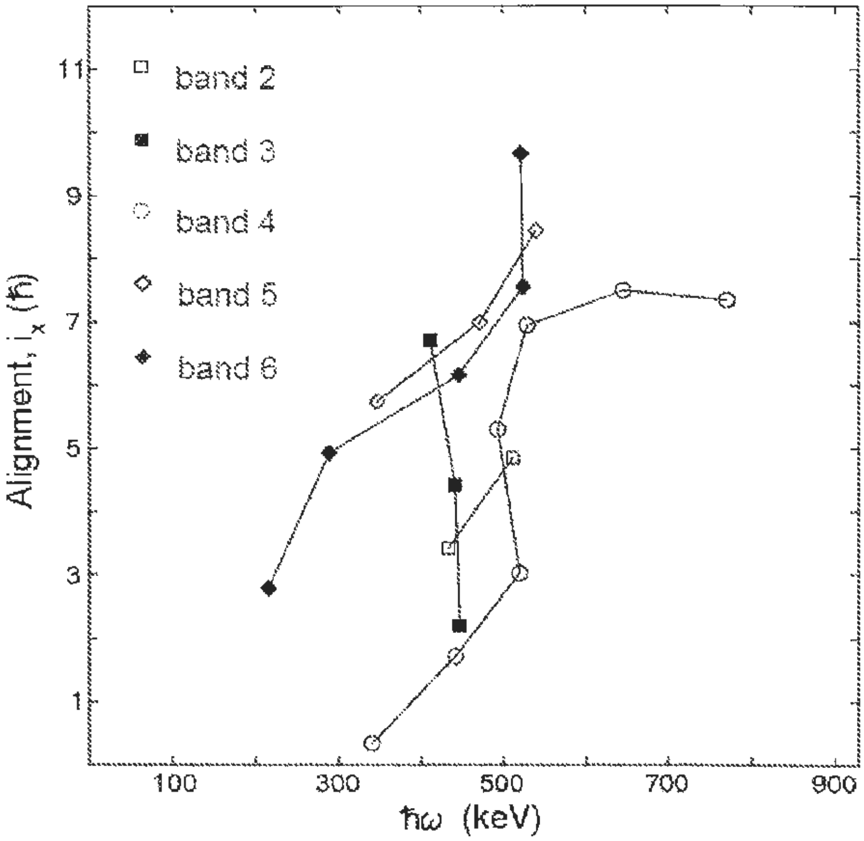

Figure 20: Alignment i_x *vs.* rotational frequency $\hbar\omega$ for bands 2-6. The Harris parameters used were $\mathcal{J}_0 = 2\frac{\hbar^2}{\text{MeV}}$ and $\mathcal{J}_2 = 10\frac{\hbar^4}{\text{MeV}^3}$.

6.2.3 Band 4

The structure underlying the ground state band (band 4) is considered to be "intermediate between a vibrator and a rotor" [14], with the deformation of the first excited 2^+ state being given by $\beta_2 = 0.074$ [22], or $\beta_2 = 0.242$ [23]. The major controversy in ^{72}Ge is that both prolate and oblate deformation have been suggested for the ground state band (refs. [3, 53] and [54-57] respectively.)[7]

The Projected Shell Model (PSM) calculations for the ground state band [3] predict a single backbend at I=6$\hbar$ for an oblate intrinsic shape of the ground state, and for the case of a prolate ground state they predict a second backbend at I=14$\hbar$ (see Fig. 22).

In the PSM calculations of [3], when the intrinsic shape is prolate, the first backbend is described by a crossing with the 2 quasi-particle (qp) band $2\nu g_{\frac{9}{2}}\left[-\frac{3}{2};\frac{5}{2}\right]$ $(K = 1)$ (where the values in square brackets indicate the m_j of the quasiparticle states); equivalently, by alignment of 2 quasi-neutrons such that they enter this configuration. For prolate deformation, there is then a second alignment involving four quasi-particles and the configurations $2\nu g_{\frac{9}{2}}[-\frac{3}{2},\frac{5}{2}] + 2\pi g_{\frac{9}{2}}[\frac{1}{2},-\frac{3}{2}](K = 0)$ and $2\nu g_{\frac{9}{2}}[-\frac{3}{2},\frac{5}{2}] + 2\pi g_{\frac{9}{2}}[-\frac{1}{2},-\frac{3}{2}](K = 1)$ [3].

In the oblate case, there is only a single backbend at $J \approx 6\hbar$, which involves alignments of four quasi-particles into the configurations $2\nu g_{\frac{9}{2}}[\frac{5}{2},\frac{5}{2}], (K = 0); 2\nu g_{\frac{9}{2}}[-\frac{7}{2},-\frac{3}{2}], (K = -2); 2\nu g_{\frac{9}{2}}[-\frac{7}{2};\frac{5}{2}], (K = -1)$, and $2\nu g_{\frac{9}{2}}[\frac{9}{2},-\frac{7}{2}], (K = 8)$ [3].

As the 14^+ level had not been previously observed, deciding between the

---

[7] The paper [59] offers a good review of the propositions for the structure of the ^{72}Ge ground state band.

prolate or oblate shape based on these predictions was somewhat difficult. A plot of $\frac{\mathcal{I}}{\hbar^2}$ with $\hbar\omega$ was made for the ground state band up to $I = 14\hbar$, using the equations for even-even nuclei [26]:

$$\begin{aligned} \frac{\mathcal{I}}{\hbar^2} &= \frac{2I-1}{E_I - E_{I-2}} \\ \hbar\omega &\approx \frac{\Delta E}{\Delta\sqrt{I(I+1)}} \Big|_{I-2}^{I} \rightarrow \frac{1}{2}(E_I - E_{I-2}). \end{aligned} \tag{32}$$

The energies measured up to $I = 14\hbar$ as in Fig. 13, were used. The resulting plot is provided below (Fig. 21); and shows a single, large backbend occurring at $(\hbar\omega)^2 \approx 0.3$ MeV^2, which is equivalent to $I \approx 6\hbar$. Thereafter, the plot follows an almost-linear shape.

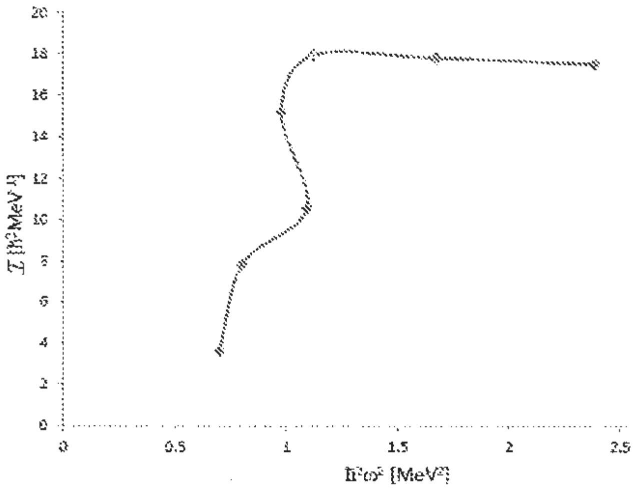

Figure 21: Plot of $\frac{\mathcal{I}}{\hbar^2}$ vs $(\hbar\omega)^2$ for the ground state band. Note single backbend at $(\hbar\omega)^2 \approx 0.3$ MeV^2.

As there is only a single backbend observed in the plot (Fig. 21), it is assumed from the PSM results [3] that the shape of the underlying structure

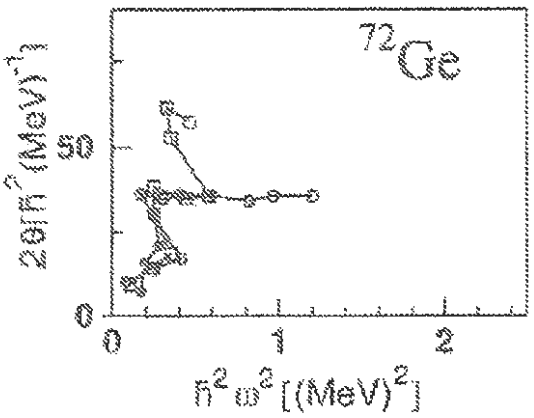

Figure 22: Backbending plot for the ground state band, predicted using PSM calculations [3]. The open circles show the predicted curve if the intrinsic shape is oblate; the open squares if it is prolate. The filled circles are the data-points up to $I \approx 8\hbar$ (data from [61]).

is predominantly oblate.

There is also, however, an argument [60] that prolate and oblate shapes coexist in the ^{72}Ge ground state band. This argument agrees with the potential energy surface for the ground state (Fig. 23), which has minima for both prolate and oblate deformation, and can explain an apparent triaxiality (the measured value for γ for the ^{72}Ge ground state band is $\gamma = 28^o$ [63]). The coexistence of prolate and oblate shapes gives the nucleus such an apparent triaxiality, because the prolate shape ($\gamma = 0°$) and oblate shape ($\gamma = 60°$) coexisting equally will give rise to a value of $\gamma \approx 30°$ [60].

Our study suggests that the ground state deformation is predominantly oblate. How the measured $\gamma \approx 28°$ may be reconciled with the potential energy surface and the triaxiality is perhaps a matter for further experimentation, since a predominantly oblate ground state would rule out the suggestion that $\gamma \approx 28^\circ$ comes about because of shape coexistence.

There are two possible explanations for the observations regarding the structure of the ground state band. Firstly, perhaps two band-crossings occur at $I \approx 6\hbar$: one which corresponds to the alignment in the prolate case, and another, which predominates, that corresponds to the oblate alignments. Thus, the nuclear ground state would have to be mainly oblate, but with a small prolate admixture. The $\gamma \approx 28^\circ$ would require an $\approx 50\%$ admixture of prolate behaviour in order for shape coexistence to explain it, however, (since an equal weighting of $\gamma = 60^\circ$ and $\gamma = 0^\circ$ shapes would give $\gamma \approx 30^\circ$), so the problem of explaining this triaxiality still exists if this is the case.

The second possible explanation, considering the potential energy surface for the ground state (Fig. 23), is that the yrast band is based on a vibration in which the nucleus vibrates between a prolate and an oblate shape. This could occur with two equally-deep minima in the potential-energy surface, as observed here: both the prolate and oblate shapes could be equally-favoured, and the nucleus could vibrate between them. If the nucleus was undergoing such a vibration it would necessarily be triaxial at some point, which would account for the measured $\gamma \approx 28^\circ$. The vibrational nature of the initial yrast states is well-known, with the E_{4^+}/E_{2^+} ratio of 2.07 being characteristic of a vibrator (since a rotor would require a ratio of 3.33). This suggestion is backed up by theoretical calculations by [64], which assume a ground state vibration arising from a superposition of an oblate and a prolate deformation. These calculations are known for their accurate reproduction of the 0_2^+ energy [10] and so seem reflective of actual structure.

Such a quadrupole vibration would be based on the p- and f- orbits, as they have $\Delta l = 2$, and are of the same parity. It is known that in the ^{72}Ge ground state, the $p_{\frac{3}{2}}$ and $f_{\frac{5}{2}}$ orbits have almost equal probablilty of occupancy (see Table 7). This equal probablility of occupancy, or mixing of these orbitals with equal weighting, would lead to the vibration of the valence nucleon density from one state to the other, and give rise to a quadrupole vibration. The calculations by [64] couple the vibration to a quasi-proton in the $p_{\frac{3}{2}}f_{\frac{5}{2}}$ orbits, and a quasi-neutron in the $p_{\frac{1}{2}}$ orbit, in agreement with these assumptions.

At an oblate deformation of $\epsilon_2 \approx -0.2$, the proton Fermi level is very close to the Nilsson orbits $[303]\frac{5}{2}$ & $[321]\frac{1}{2}$. Thus the occupation probability for these orbitals is expected to be about equal. At this deformation, the neutron Fermi level is close to $[301]\frac{3}{2}$ & $[413]\frac{7}{2}$. Similarly, an equal occupational probability for the orbits $[310]\frac{1}{2}$ & $[312]\frac{3}{2}$ is expected at a *prolate* deformation of $\epsilon_2 \approx +0.2$, while the neutron Fermi level lies close to $[422]\frac{5}{2}$ & $[301]\frac{1}{2}$ & $[303]\frac{5}{2}$ (the $[301]\frac{1}{2}$ & $[303]\frac{5}{2}$ being nearly degenerate at this deformation). These must be the orbitals associated with the oblate and prolate shapes, respectively, since the potential well has a minimum at both these ϵ_2 values.

Table 7: The occupancies for the valence orbitals in the ground state of ^{72}Ge [65].

Protons		Neutrons	
Orbital	Occupancy	Orbital	Occupancy
$f_{\frac{5}{2}}$	1.98	$f_{\frac{5}{2}}$	3.87
$p_{\frac{1}{2}}$	0.38	$p_{\frac{1}{2}}$	0.98
$p_{\frac{3}{2}}$	1.63	$p_{\frac{3}{2}}$	3.27
$g_{\frac{9}{2}}$	0	$g_{\frac{9}{2}}$	3.88

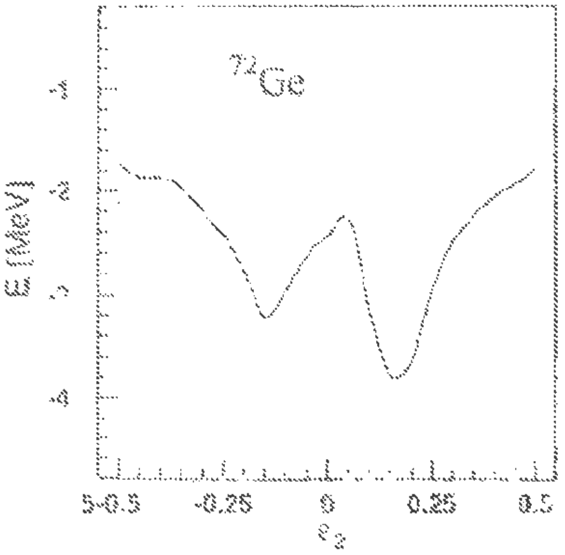

Figure 23: The potential-energy surface for the ground state of ^{72}Ge. Note the minima at prolate and oblate deformation [3].

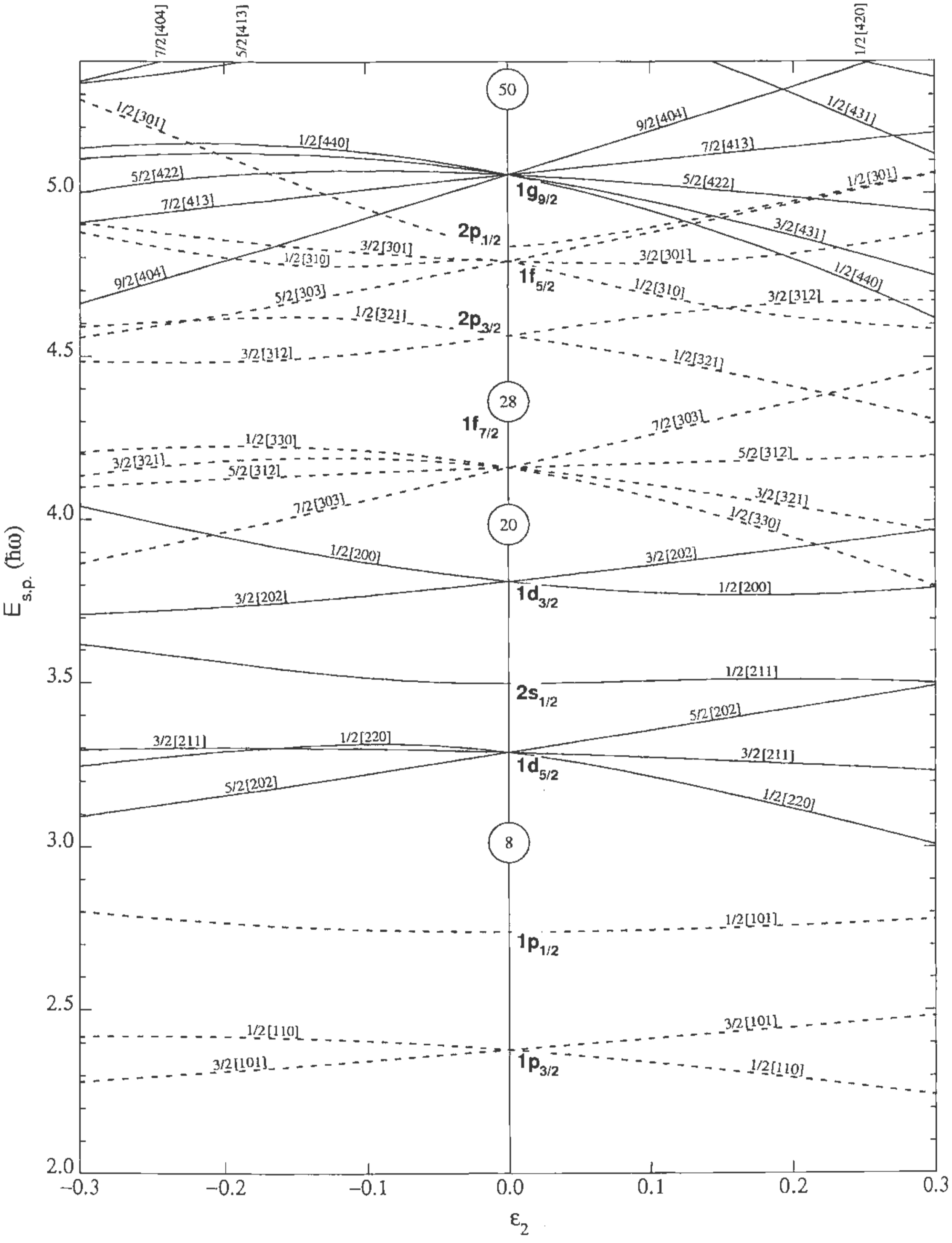

Figure 24: Nilsson diagram for N or $Z \leq 50$ [30]. Note equal probabilities of occupancy for $[303]\frac{5}{2}$ and $[321]\frac{1}{2}$ orbits for $\epsilon_2 \approx -0.2$, and for $[303]\frac{5}{2}$, $[321]\frac{1}{2}$ and $[422]\frac{5}{2}$ orbits for $\epsilon_2 \approx 0.2$.

6.2.4 Bands 5 and 6

It may be observed from plots of alignment *vs.* rotational frequency (Fig. 20) that, except at high spins, bands 5 and 6 have almost parallel alignment patterns. This suggests that they have similar underlying structure. This suggestion is supported by the plot of excitation energy *vs.* spin for these bands (Fig. 19), which show that they have very similar excitation energies.

The plot of excitation energy *vs.* spin I (Fig. 19) also shows that the lowest level of band 5–at 3.249 MeV–does not lie on a smooth curve. This suggests that the 3.249 MeV level may not belong to this band; or if it does, it is strongly mixed with a different configuration.

The high-frequency part of band 6 shows a sharp alignment gain (Fig. 20). This must correspond to the alignment of a pair of quasiparticles (pair-breaking).

Bands 5 and 6, when considered as being based on the same underlying structure, have characteristics of an octupole vibrational band: they are both odd-parity, and, since band 5 is even-spin and band 6 is odd-spin, they form a "ladder" of states with $\Delta I = 1$ between the two bands. The alternating levels of $\Delta I = 1$ are linked by inter-band $M1/E2$ transitions with a strong quadrupole admixture (see Table 8). Thus, it is proposed here that bands 5 and 6 are part of an octupole vibrational band, based on the known 1-phonon octupole vibration underlying the 3_1^- level at 2.515 MeV.

This interpretation fits well with known facts about ^{72}Ge: The existence of a vibrational band on the 2.515 MeV 3^- level would agree with the suggestion that this level is very strongly collective, as has been noted (*e.g.* by [4]). As mentioned above, the 3_1^- level is interpreted as an octupole vibration. If the nucleus then rotates, in addition, a band arises with an almost

Table 8: Values of mixing ratio (δ) for the inter-and intra-band transitions of band 5.

intra-band transitions			
Transition	between levels	Character	δ
580	$6^- - 5^+$	$M1/E2$	0.32
760	$8^- - 6^-$	$E2$	
997	$10^- - 8^-$	$E2$	
1120	$12^- - 10^-$	$E2$	
inter-band transitions			
Transition	between levels	Character	δ
699	8^-(band 5)-7^-(band 6)	$M1/E2$	-0.84
748	6^-(band 5)-5^+(band 3)	$E1$	0.27
803	8^-(band 5)-7^-(band 6)	$M1/E2$	-0.84 or -1.73
843	10^-(band 5)-9^-(band 6)	$M1/E2$	0.27
1056	6^-(band 5)-6^+(band 4)	$E1/M2$	0.36
1520	5^+(band 5)-4^+(band 4)	$M1/E2$	0

linear pattern in $E/(I(I+1))$, exhibiting both even- and odd-spin sequences.

Such a structure (one odd-spin and one even-spin band, linked with $\Delta I = 1$ transitions), is also indicative of deformation-aligned coupling [28].

It is worth noting that a similar structure (an octupole vibrational band with both odd- and even-spin bands of negative-parity) was identified in another "tetrahedral candidate" ^{160}Yb, in the recent study by Bark *et al.* [12]. That there was also vibrational octupole deformation in this nucleus seems less of a coincidence and more of a suggestion that tetrahedral deformation, if such exists, is liable to be vibrational rather than static.

The identification of band 6 as part of a vibrational band indicates that the octupole behaviour associated with the 2.515 MeV level is highly collective, although not static as has been suggested [4]. Since this octupole vibration is based on the $g_{\frac{9}{2}}$ orbitals, it may be concluded that these are especially lowered in energy in this nucleus in order to make the octupole behaviour so strongly collective.

The octupole vibration underlying the 3_1^- state would occur as a result of the $g_{\frac{9}{2}}$ orbital being very low-lying in this nucleus [8]: the $g_{\frac{9}{2}}$ orbit would be the unique-parity orbit in the fp-shell, separated from the surrounding orbits by $\Delta I = 3$: the structure described by [4] to underlie octupole vibrations. Octupole collectivity occurs when the octupole component of the mean field couples these unique-parity and common-parity orbits separated by $\Delta I = 3$. This phenomenon is predicted to occur at the proton or neutron numbers N or $Z \approx 34$, 56, 88 and 134, since these nucleon numbers make the octupole component of the mean field particularly strong [51].

The IBA calculations of [4] suggest that the 3_1^- level at 2.152 MeV is based on an interacting-boson system of 10 s-d bosons and one f-boson. This f-boson would give rise to the underlying octupole vibration. It is interesting to observe that when nucleons occupy these orbitals (the $1g_{\frac{9}{2}}$ and $2d_{\frac{3}{2}}$ orbitals), a strong pairing occurs, giving an f-boson rather than two disparate fermions. Why this increased likelihood of pairing should occur in this circumstance is a question worth considering.

As regards the effect of proton-neutron ratio on (ground state) nuclear properties, it is especially interesting to note that the complicated variation in ground state deformation with N shown by the $Z = 32$ nuclei does not occur to nearly the same degree in the $Z = 34$ isotopes [54]: that is, all selenium isotopes studied by [54] appeared to exhibit similar behaviours, but there is a drastic changeover in behaviour around $N = 40$ exhibited by the germanium nuclei. This must suggest the variation in shape is due to p-n interaction (as suggested by [8]) and not purely due to the opening of a shell-gap at N=40, since there is no major change in the behaviour of selenium when N=40.

7 Conclusion

The level scheme of ^{72}Ge has been extended by 27 transitions, and the placement of 11 transitions has been altered from that in the previous level scheme. Two new structures have been added to the level scheme, and the spins and parities of 7 levels have been determined via the PDCO method. The spin and parity of two previously-known levels have been changed.

Through the extension of the yrast band to the 14^+ level and comparison of its backbending behaviour with projected shell model predictions, it has been concluded that the ground state of ^{72}Ge may be predominantly oblate. How this observation ties in with the measured eccentricity $\gamma \approx 28°$ and suggested shape coexistence [60] is a question which it may take further experimentation to answer.

A new structure added to the level scheme was identified as being part of an octupole vibrational band, based on the known one-phonon octupole vibration at 2.515 MeV. The existence of this band is consistent with predictions that the octupole behaviour associated with this level is highly collective, although not static, as has been suggested in the past [4]. Since this octupole vibration is based on the $g_{\frac{9}{2}}$ orbitals, it may be concluded that these are especially lowered in energy in this nucleus, in order to make this octupole behaviour so strongly collective.

The octupole vibration and backbending behaviour observed in this nucleus confirm the importance of both the neutron and proton $g_{\frac{9}{2}}$ orbitals at $(N,Z) = (40,32)$, and demonstrate how lowered in energy these orbits are with this N and Z. In neighbouring isotopes, this lowering is not observed for both the neutron and proton $g_{\frac{9}{2}}$ orbitals (*e.g.* ^{70}Ge, $\left\langle n g_{\frac{9}{2}} \right\rangle \simeq 0$ [65]). Thus, since large proton $g_{\frac{9}{2}}$ occupancy (~ 0.5) is believed to have its origin in strong p-n interactions [8], this suggests that there is a particularly strong

p-n interaction at $(N,Z) = (40,32)$.

The failure to observe tetrahedral states in this data-set may be ascribed to their being particularly long-lived, or not being populated in this reaction. However, it may also be suggested, since an octupole vibrational band was observed, as in studies on other tetrahedral candidates, that tetrahedral shapes may be vibrational rather than static, due to their being reflection-asymmetric. The need for α-clusters to create a reflection-asymmetric mean field has been questioned in this regard. It has therefore been suggested that ^{40}Ca may be a possible tetrahedral candidate.

In overview, then, it has been determined that the ^{72}Ge nucleus shows highly-collective (although not static) octupole behaviour, and that, like its ground state deformation, this is heavily influenced by the lowering of both the proton and neutron $g_{\frac{9}{2}}$ orbitals. Many of the other macroscopic properties of ^{72}Ge *e.g.* alignments and backbending, have also been observed to be based on these orbitals, which may thus be concluded to perform a very important role in this nucleus.

8 Appendix

8.1 Appendix 1: Data-structures

The data "matrices" are two- or higher-dimensional arrays in which each array coordinate is incremented for a coincidence. The array thus functions like a histogram with two or more criteria for incrementing each bin: that is, "bin AB" would be incremented whenever transition "A" is detected within the same coincidence window as transition "B", making the two criteria that both transition A and transition B were detected within the same interval.

The number of counts in the bin would correspond to the intensity of this coincidence. Each transition is specified by its energy, so a matrix such as that described above would have energy-values on both "axes", and is thus referred to as a "symmetric matrix" (since both bin AB and bin BA would be incremented equally). Imposing additional criteria, such as requiring that the coincidences be between transitions recorded at different polar angles, may result in "asymmetric" matrices. Histograms for classifying transitions (*i.e.* DCO and polarisation anisotropy matrices) are of the latter type: *e.g.* coincidences between "A" measured at $\theta = 90°$ and "B" measured at $\theta = 135°$ would be binned in bin AB for an asymmetric DCO matrix.

A vertical or horizontal slice through a two-dimensional histogram will produce a 1-dimensional spectrum showing the number of counts with which the particular transition is seen in coincidence with any other in the histogram. To take such a slice is referred to as "gating", and setting such a gate gives the coincidence spectrum for a transition.

A three- or higher-dimensional symmetric histogram may be used for large data-sets: these essentially have three or more criteria for every bin: *e.g.* "bin ABC" would be incremented for each coincidence event of transition A with transition B, and also for transition C with B. Three transitions may thus be placed within the same band structure if a high "triple coincidence" is recorded.

The process of sorting essentially requires "scanning" the raw data on an event-by-event basis. Every event contains a record of which detectors fired and the corresponding ADC channel number, time and bit-pattern. The scanning occurs via an input-code.

Upon encountering a coincidence signal with the energy and time signals specified by the input code, the software will increment the relevant data-structure, which is displayed either as a spectrum or as a "map" depending on whether the data-structure is one- or two-dimensional. Histograms of one or two dimensions may be produced, with further steps required for the sieving off of triple- or higher-order- coincidence events [43].

8.2 Appendix 2: Gain-drift correction

The spectrometer array will not behave consistently or identically over the course of an experiment. This is because there are unavoidable fluctuations in temperature in the experimental vault that will affect the performance of the individual amplifiers and cause the voltage associated with a particular energy to "drift" over time. Correction for these random errors ("gain-drift" correction) is thus required during data-sorting.

The energy-values assigned in one run to one recorded high-energy and one recorded low-energy transition are selected as standards, and the difference between these chosen values and the energy-values assigned is plotted for each detector and each run. It is assumed that the recorded "drifts" in the energies of the chosen standard transitions apply to all neighbouring energies.

These drift values are incorporated into the sorting program to compensate for drift in each run.

8.3 Appendix 3: Classifying transitions

Angular distribution and multipolarity

Angular distribution of intensity of a transition of multipolarity $\lambda + \lambda'$ with a mixing ratio of $\delta(\gamma)$, from a state of angular momentum I_i to one of $I = I_f$ is given by [48]:

$$W(\theta, \phi) = \sum_{k_i,q_i} \rho_{k_i q_i}(I_i)\sqrt{(2k_i+1)}A_{k_i}(\delta_{\gamma if}\lambda\lambda' I_f I_i)Q_{k_i}(E_{\gamma if})D^{k_i *}_{q_i 0}(\theta_i, \phi_i, 0), \tag{33}$$

where θ_i and ϕ_i are the polar and azimuthal angles at which the intensity is being observed (defined with respect to the beam line, as in Fig. 12 [27]) and $\delta_{\gamma if}$ is the mixing ratio of the transition in question. The I_i and I_f are the angular momenta of the initial and final states. The remaining functions are defined in [48], and A_{k_i} is essentially a ratio of the F-coefficient for the transition (which expresses the coupling of the angular momenta involved) and the mixing ratio $\delta_{\gamma if}$. The $Q_{k_i}(E_{\gamma if})$ expresses the solid-angle opening of the detector, $D^{k_i *}_{q_i 0}(\theta_i, \phi_i, 0)$ is the rotation matrix (about the beam line), and k_i and q_i are integer labels for the transition, with the values: $k_i = 0, 1, 2...2I_i$ (for I_i integer; upper limit $2I_i - 1$ if I_i is half-integer), and $q_i = -k_i, -k_i + 1...k_i$. The statistical tensor $\rho_{k_i q_i}$ gives the orientation of the initial state [48].

Polarisation

When two elements of the same detector fire in immediate succession, (as occurs in a scattering event), the event is assigned a value which is the sum of the relevant bit-values (see Fig. 6 for the values). When the detectors are oriented in a known way, this allows the scattering-direction to be identified.

Conventionally, the Clover detectors are oriented in an array such that, no matter where they are placed, the "bit-value = 1" and "bit-value = 2" elements make the smallest angle with the beam-line (see Fig. 8). Thus, a bit-pattern of 10 and 8 are indicative of horizontal scattering events and bit patterns of 3 and 12 indicate vertical scattering.

The polarisation-sensitivity curve $Q(E)$ for a Clover detector was determined by [36] as:

$$Q = Q_0 \times \left\{0.31(2) + 7(2) \times 10^{-5} \times E_\gamma[\text{keV}]\right\} \tag{34}$$

where the value Q_0 is the polarisation sensitivity of an ideal Compton polarimeter and is given by [36]:

$$Q_0 = \frac{1+\alpha}{1+\alpha+\alpha^2}, \tag{35}$$

with $\alpha = E_\gamma[\text{keV}]/511$.

As there is an uncertainty in the value of Q (Eqn 34), the uncertainties in measured values of polarisation E_P were determined via

$$E_P = P \times \sqrt{\left(\frac{E_V}{N_V}\right)^2 + \left(\frac{E_H}{N_H}\right)^2 + \left(\frac{E_Q}{Q}\right)^2}, \tag{36}$$

where E_V and E_H indicate the experimental uncertainty in the measured intensities (from RadWare output), and E_Q is the uncertainty in Q, as supplied by Eqn 34 [36].

References

[1] J. Dudek *et al.*, J. Phys. G: Nucl. Part. Phys. **37**, 2010.

[2] J. Dudek *et al.*, Phys. Rev. C **88**, 502, 2002.

[3] P. A. Dar *et al.*, Phys. Rev. C **75**, 315, 2007.

[4] D. S. Chuu *et al.*, Phys. Rev. C. **47**, 183, 1993.

[5] B. Kotlinski *et al.*, Nucl. Phys. A **519**, 646, 1990.

[6] F. J. Kline *et al.*, Nucl. Phys. A, **225**, 435, 1975.

[7] A. C. Rester *et al.*, Nucl. Phys. A **346**, 371, 1980.

[8] M. Hasegawa *et al.* Nucl. Phys. A **789**, 46, 2007.

[9] P. D. Cottle, Z. Phys. A: Hadrons and Nuclei **338**, 281, 1991.

[10] C. Morand *et al.*, Nucl. Phys. A. **313**, 47, 1979.

[11] S. Shen *et al.*, Int. J. Mod. Phys. E, **17**, no. 6, 1061, 2008.

[12] R. A. Bark *et al.*, Phys. Rev. C **104**, 501, 2010.

[13] T. Kibedi and R. H. Spear, Atomic Data and Nuclear Tables **80**, 35, 2002.

[14] S. Shen *et al.*, J. Phys. Soc. Jpn **74**, 229, 2005.

[15] H. Schuler and T. Schmidt, Th. Z. Physik **94**, 457, 1935.

[16] A. Bohr and B. R. Mottelson, "*Nuclear Structure (Vol. II: Nuclear Deformations)*", World Scientific Publishing, Singapore, 1998. Pp 4-9.

[17] K. Heyde, "*Basic Ideas and Concepts in Nuclear Physics: An Introductory Approach*", (3^{rd} ed.), Institute of Physics publishing, Bristol, 2004. Pp 408-414.

[18] D. J. Brink *et al.*, J. Phys. G: Nucl. Phys. **13**, 24, 1987.

[19] J. Dudek *et al.*, arXiv: Nucl. Th. **1**, 1, 2002.

[20] J. Dudek *et al.*, Phys. Rev. C **97**, 501, 2006.

[21] L. Reidinger, "*E1 Rates and Things Tetrahedral*", unpublished (27/08/2008).

[22] S. Raman *et al.*, Atomic Data and Nuclear Tables **42**, 1, 1989.

[23] S. Raman *et al.*, Atomic Data and Nuclear Tables **78**, 1, 2001.

[24] R. Lecomte *et al.*, Nucl. Phys. A **284**, 123, 1977.

[25] R. F. Casten, "*Nuclear Strucure from a Simple Perspective*", (2^{nd} ed.), Oxford University Press, Oxford, 2000. Pp 10-15, 97-100, 163-168, 173-197 and 252-255.

[26] S. S. M. Wong, "*Introductory Nuclear Physics*", Pearson Prentice-Hall publishing, New Jersey, 2002. Pp261-274, and 372-375.

[27] K. S. Krane, "*Introductory Nuclear Physics*", J. Wiley and Sons publishing, Singapore, 1988. Pp 134-149 and 333-334.

[28] P. H. Reagan, "*Post-Graduate Nuclear Experimental Techniques*", Course notes for 4NET course, University of Surrey, 2003. Pp 7-9, 17-20 and 25-30.

[29] S. Karatagildis, private communication (03/02/2011).

[30] S. G. Nilsson and I. Ragnarsson, "*Shapes and Shells in Nuclear Structure*", Cambridge University Press, Cambridge, 1995. Pp 1-15

[31] J. D. Garrett, "*Shape and Pair Correlations in Rotating Nuclei*", Lectures presented at the International School of Heavy Ion Physics; Second course, Erice, Italy, 1986.

[32] N. A. Jelley, "*Fundamentals of Nuclear Physics*", Cambridge University Press, Cambridge, 1990. Pp 240-243.

[33] A. Johnson *et al.*, Phys. Lett. B. **34**, 605, 1971.

[34] J. Dudek, private communication (20/06/2010).

[35] H. Feldmeier, private communication,(22/05/2011).

[36] K. Starosta *et al.*, Nucl. Inst. Meth. in Phys. Re. A **423**, 16, 1999.

[37] A. Korichi *et al.*, Phys. Rev. C **86**, 2746, 2001.

[38] N. Shunck and J. Dudek, Int. J. Mod. Phys. E **86**, 1, 2008.

[39] G. F. Knoll, "*Radiation Detection and Measurement*", (3^{rd} ed.), J. Wiley and Sons publishing, Singapore, 2000. Pp 62-70, 79-81 and 306-311.

[40] P. M. Jones, Nucl. Instr. and Meth. A **362**, 556, 1995.

[41] G. Duchêne *et al.*, Nucl. Instr. and Meth. A **432**, 90, 1999.

[42] D. G. Roux, PhD Thesis, University of Cape Town, 2001.

[43] J. Cresswell and J. Sampson, *MTSort Manual*, unpublished (accessed at http://ns.ph.liv.ac.uk/MTsort-manual/MTsort.html), (21/01/2010).

[44] D. C. Radford, Nucl. Inst. Meth. A **361**, 306, 1995.

[45] *The RadWare Directory of Level-Schemes*, (D. C. Radford) (accessed at http://radware.phy.ornl.gov/agsdir1.html) (15/06/2010).

[46] R. A. Bark, private communication (21/10/2010).

[47] Ch. Droste *et al.*, Nucl. Inst. and Meth. A **378**, 518, 1996.

[48] A. E. Stuchbery, Nucl. Phys. A **723**, 69, 2003.

[49] A. Krämer-Flecken *et al.*, Nucl. Inst. Meth. in Phys. Re. A **275**, 333, 1988.

[50] R. A. Bark, unpublished.

[51] S. Åberg *et al.*, Annu. Rev. Nucl. Part. Sci. **40**, 439, 1990.

[52] T. Inakura *et al.*, Nucl. Phys. A. **710**, 261, 2002.

[53] J. Döring *et al.*, Phys. Rev. C **57**, 2912, 1998.

[54] R. Lecomte *et al.*, Phys. Rev. C **22**, 2420, 1980.

[55] K. Kumar, J. Phys. G **4**, 849, 1978.

[56] E. F. Aguilera *et al.*, Phys. Lett. B **201**, 22, 1988.

[57] E. F. Aguilera *et al.*, Phys. Rev. C **52**, 3103, 1995.

[58] Z. F. Muhammad *et al.*, Phys. Rev. C **81**, 609, 2010.

[59] D. Ardouin *et al.*, Phys. Rev. C **18**, 2739, 1978.

[60] W. Andrejtscheff and P. Petkov, Phys. Lett. B **329**, 1, 1994.

[61] B. L. Cohen, "*Concepts of Nuclear Physics*", McGraw-Hill publishing, New York, 1971. Pp 110-115.

[62] S. Sugawara *et al.*, Eur. Phys. J. A. **16**, 409, 2003.

[63] F. Ballester *et al.*, Nucl. Phys. A **490**, 227, 1988.

[64] M. Didong *et al.*, Phys. Rev. C **14**, 1189, 1976.

[65] B. A. Brown, unpublished.